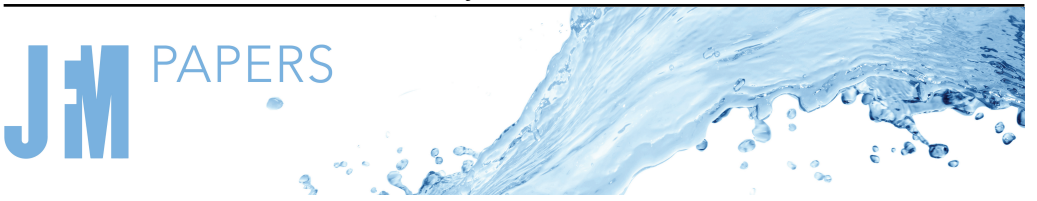
J. Fluid Mech. (2026), *vol.* 1034, A14, doi:10.1017/jfm.2026.11449



Asymmetric shock reflection in supersonic overexpanded jet

Boyuan Liu[1], **Zhudi Li**[1] **and Chenyuan Bai**[1]

[1]Ministry of Education Key Laboratory of Fluid Mechanics, Beihang University, Beijing 100191, PR China

Corresponding author: Chenyuan Bai, baicy@buaa.edu.cn

(Received 31 December 2025; revised 16 March 2026; accepted 16 March 2026)

This paper investigates asymmetric shock reflection in a supersonic overexpanded jet. A theoretical model that can predict the size and shape of flow field structures such as shocks, expansion waves and sliplines is established. For symmetric Mach reflection, the current model exhibits better agreement with numerical simulation results. For asymmetric Mach reflection, the current model also shows good agreement with numerical simulation results in predicting Mach stem height. The research indicates that the Mach stem height decreases with increasing nozzle pressure ratio and nozzle exit length difference, and decreases as the nozzle exit Mach number decreases. In addition, the critical geometric condition for complete misalignment of the upper and lower slipline interference segments (i.e. when the interference between one side of the expansion wave and the slipline ends, the other side of the expansion wave has not yet begun to interfere with the slipline) is given, which increases approximately linearly with nozzle pressure ratio and decreases as the nozzle exit Mach number increases. This study provides important theoretical support for the engineering application of asymmetric shock reflection in supersonic overexpanded jet.

Key words: high-speed flow, shock waves, supersonic flow

1. Introduction

Shock reflection is a critical physical phenomenon, widely observed in both internal and external flow fields of aircraft. For supersonic aircraft engines, shock reflection is present at the lip of the inlet (Häberle & Gülhan 2007; Xie *et al.* 2018; Sun *et al.* 2024; Tang *et al.* 2025*b*), within the internal flow (Onofri & Nasuti 1999; Huang *et al.* 2020; Wu *et al.* 2025)

© The Author(s), 2026. Published by Cambridge University Press.

https://doi.org/10.1017/jfm.2026.11449 Published online by Cambridge University Press

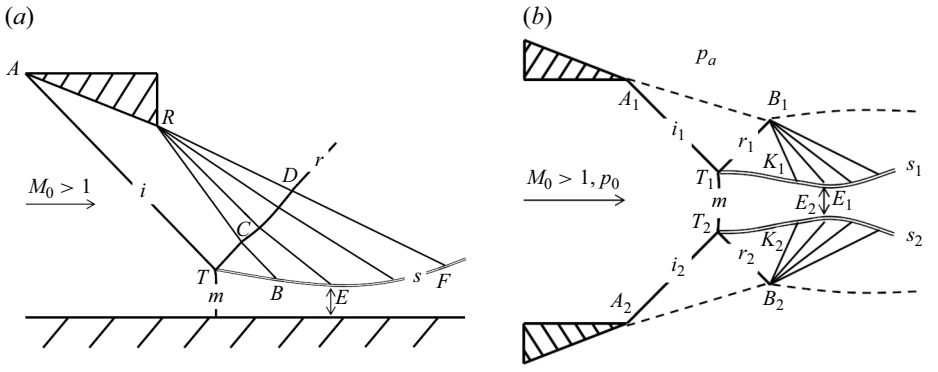


Figure 1. Schematic illustration of shock reflection. (*a*) Wedge flow shock reflection. (*b*) Overexpanded jet shock reflection. Here, *i* represents incident shock, *r* represents reflected shock, *s* represents slipline and *m* represents Mach stem.

and in the jet downstream of the nozzle exit (Powell 1953; Arun Kumar & Rajesh 2017; Li *et al.* 2024); by changing flow field parameters, it affects the engine's performance and efficiency. Therefore, a deeper understanding of shock reflection will contribute to the design of higher-performance engines.

Two typical flow field structures of shock reflection are shown in figure 1. Figure 1(*a*) presents the shock reflection flow field structures of the incident shock generated by the wedge surface (wedge flow shock reflection) and figure 1(*b*) shows the shock reflection flow field structures of the incident shock caused by high ambient pressure (overexpanded jet shock reflection) (Hadjadj, Kudryavtsev & Ivanov 2004; Wu *et al.* 2025).

For wedge flow shock reflection, the research on flow structures is relatively well established. Classical studies include shock reflection types (regular reflection (RR) and Mach reflection (MR) (Mach 1878)), the triple-shock theory for the solution of flow parameters near the triple point (von Neumann 1945), critical conditions (detachment criterion and von Neumann criterion (von Neumann 1943)) and hysteresis phenomena (Henderson & Lozzi 1975; Hornung, Oertel & Sandeman 1979; Vuillon, Zeitoun & Ben-Dor 1995; Ivanov *et al.* 2001; Ben-Dor *et al.* 2002). In addition, scholars have also conducted detailed discussions on the multiple incident shock reflections (Ben-Dor, Dewey & Takayama 1987; Guan *et al.* 2018, 2020; Meng *et al.* 2017; Li & Bai 2025), curved shock reflection (Shi *et al.* 2023; Zhang *et al.* 2023; Yan *et al.* 2024; Tian 2024) and the shock reflection in axisymmetric flow (Ji *et al.* 2019; Zhang *et al.* 2024; Shoesmith & Timofeev 2025). The influence of trailing edge height on Mach stem height (Bai & Wu 2021), centred compression wave reflection (Bai 2024), strong Mach reflection (Qin *et al.* 2022), the Mach reflection when the expansion wave at the wedge tail disturbs the incident shock wave (Bai 2023), shock reflection over curved wedge (Wang *et al.* 2017, 2021, 2022), and interaction between centred-compression waves and cowl shock (Tang *et al.* 2025*a*) have also been studied.

For symmetric wedge flow shock reflection, an analytical solution model for flow field structures is a significant research focus. The commonality of the solution is that they all use classical quasi-one-dimensional flow theory to analyse the flow below the slipline. The model of Azevedo & Liu (1993) assumed that the sonic throat is located at the turning point (*B* in figure 1*a*) where the slipline is disturbed/undisturbed by the leading characteristics line. The model of Li & Ben-Dor (1997*a*) allowed the sonic throat to be determined by the transmitted expansion wave, using the assumption that the flow just above the sonic throat is parallel to the free stream flow. The model of Mouton & Hornung (2007) assumed that

https://doi.org/10.1017/jfm.2026.11449 Published online by Cambridge University Press

the sonic throat occurs further downstream and also assumed that the slipline is a straight line. Gao & Wu (2010) and Bai & Wu (2017) considered the secondary expansion waves generated on the initial segment of the slipline (*TB* in figure 1*a*) due to the pressure drop caused by the contraction of the quasi-one-dimensional isentropic flow region. In general, the differences among these models lie in the localisation of the sonic throat, assumptions about the slipline shape and consideration of secondary flow field interference. Early models mostly relied on simplified assumptions (e.g. treating the slipline as a straight line and fixing the sonic throat at a specific position), while subsequent studies gradually incorporated practical flow effects such as secondary expansion waves induced by the contraction of the quasi-one-dimensional flow field, making the models more consistent with the complex physical nature and continuously improving prediction accuracy.

For asymmetric wedge flow shock reflection, an analytical solution model for flow field structures remains a significant research focus. Tao *et al.* (2017) modelled the incident shock, reflected shock and Mach stem as straight lines, and the average flow deflection angle in the quasi-one-dimensional isentropic region as the mean of the upper and lower slipline angles – a value updated iteratively during the solution process. By incorporating the Prandtl–Meyer relation, they solved for the Mach stem height in asymmetric Mach reflection. Roy & Rajesh (2017) proposed a model that assumed the Mach stem to be a second-order curve and introduced a common horizontal symmetry axis within the quasi-one-dimensional isentropic flow region. By decomposing the asymmetric configuration into upper and lower symmetric subdomains, the model enabled the solution of asymmetric Mach reflection. Building upon this work, Roy & Gopalapillai (2019) further introduced the concept of the average flow deflection angle, defined as the mean of the streamline deflection angles induced by the Mach stem at the upper and lower triple points, which extended the model's capability to predict inverse Mach reflection (InMR) configurations. Additionally, such assumption of the average flow deflection angle in the quasi-one-dimensional isentropic flow region was similarly employed by Lin, Bai & Wu (2019). They hypothesised the Mach stem as a circular arc, and by incorporating interactions between secondary waves and the sliplines, they systematically analysed the effects of asymmetric upper and lower wedge angles, wedge lengths, and streamwise leading-edge positions on the flow field structures.

For overexpanded jet shock reflection, the reflection types, critical criteria and hysteresis phenomena are consistent with those of the wedge flow shock reflection. Their difference lies in the flow field structure. When the incident shocks are caused by high ambient pressure, the reflected expansion waves (at B_1 and B_2 in figure 1*b*) do not interfere with the reflected shocks (T_1B_1 and T_2B_2 in figure 1*b*), but directly interact with the sliplines. In addition, scholars have also conducted discussions on the hysteresis phenomenon in jet flows by experiments (Kashitani *et al.* 2003; Matsuo *et al.* 2011; Lavala & Das 2025) and CFD (computational fluid dynamics) simulations (Hadjadj *et al.* 2004; Yasunobu *et al.* 2006; Shimshi *et al.* 2009, 2015; Hew, Ogawa & Boswell 2024).

For symmetric overexpanded jet shock reflection, the analytical solution model for flow field structures is relatively well established. When considering the non-uniformity of the flow field downstream of the incident and reflected shock, the method of characteristics (MOC) can be used to establish a model for solving the flow field structures of overexpanded jet. The earliest relevant work was carried out by Ashratov (1966). Subsequently, Chow & Chang (1975) extended the solution to the case where the region downstream of the reflected shock is subsonic. Rolland *et al.* (2024) considered a more refined flow field downstream of the incident shock to solve the Mach stem height, enhancing the prediction accuracy for small Mach stems. When considering the uniformity of the flow field downstream of the incident and reflected shock, predictive

https://doi.org/10.1017/jfm.2026.11449 Published online by Cambridge University Press

models for flow field structures are also established in an overexpanded jet. Li & Ben-Dor (1997*b*) incorporated the effects of expansion waves on the jet structure. The straight lines assumption is used to model the incident shock wave, reflected shock wave, jet boundary and the part of the slipline not intersecting with the expansion wave. Additionally, the part of the slipline intersecting with the expansion wave is modelled as a curve with a small curvature. From this, they derived a theoretical predictive model for the flow field structures and size. Omelchenko, Uskov & Chernyshov (2003) investigated the interaction between the reflected shock and secondary expansion waves, predicting the Mach stem height in an overexpanded jet using an iterative approach with termination conditions based on either achieving sonic flow or flow flattening at the throat. Chernyshov, Savelova & Kapralova (2021) extended the model proposed by Omelchenko *et al.* (2003), described expansion waves based on the straight-line assumption and developed a theoretical model for the rapid prediction of the flow field structures of Mach reflection in an overexpanded jet based on flow averaging downstream of a curved Mach stem. Based on the classical shock reflection models of Li & Ben-Dor (1997*a*), Mouton & Hornung (2007) and Bai & Wu (2017). Paramanantham, Janakiram & Gopalapillai (2022) provided three revised models to solve the flow field configuration in an overexpanded supersonic jet. They also compared these revised models with experimental and numerical results to verify their validity.

For asymmetric overexpanded jet shock reflection, frequently induced by non-ideal engineering conditions, current research remains relatively insufficient. Upstream non-uniformity-induced asymmetric flow structures represent one of the key contributing factors. This issue has been preliminarily explored by Hew *et al.* (2023), who introduced Mach number non-uniformity at the inlet to solve the flow field structure of asymmetric Mach reflection. Another crucial factor is nozzle exit geometric asymmetry, which represents a common and important engineering scenario. Such geometric asymmetries may originate from numerous engineering factors: manufacturing tolerances leading to actual lip position deviations, active asymmetric designs in thrust vectoring nozzles (Lv *et al.* 2017), etc. The above-mentioned factors lead to differences in the upper and lower shock positions of the jet, thereby inducing asymmetric shock reflection. Compared with symmetric shock reflection, the throat flow deflects and the expansion wave interactions on both sides of the throat need to be considered in a coupled manner. However, a systematic theoretical modelling study on this issue is still lacking.

In general, research on the asymmetric overexpanded jet shock reflection remains relatively limited. This paper develops a theoretical model that can predict the asymmetric flow field structures in a supersonic overexpanded jet. The structure of this paper is as follows: § 2 defines the the physical scenario of asymmetric flow in an overexpanded jet, describes the numerical methods employed and analyses the flow field of asymmetric supersonic overexpanded jet with numerical results; § 3 presents the theoretical model used in this article; § 4 evaluates the theoretical model's accuracy and studies the influence of nozzle exit parameters of flow field structures; and § 5 summarises the main conclusions.

2. Numerical simulation method and flow characteristics of asymmetric shock reflection in an overexpanded jet

In this section, we first define the physical scenario of asymmetric flow in an overexpanded jet caused by nozzle geometric asymmetry. Then, we present the CFD method used here. Finally, we analyse the flow characteristics in asymmetric shock reflection in an

https://doi.org/10.1017/jfm.2026.11449 Published online by Cambridge University Press

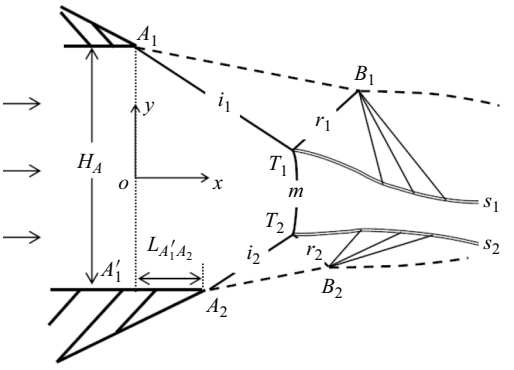


Figure 2. Schematic illustration of asymmetric Mach reflection in an overexpanded jet.

overexpanded jet based on CFD results. In this paper, the specific-heat ratio γ is 1.4 and the gas constant R is 287 J (kg K)$^{-1}$.

2.1. *Definition of asymmetric shock reflection in an overexpanded jet*

Figure 2 is a schematic illustration of asymmetric Mach reflection in an overexpanded jet. The shaded triangles represent nozzle exit geometry, where the exit velocity is aligned with the x-axis. The nozzle height A_1A_1' is H_A, nozzle exit Mach number is M_0 and nozzle pressure ratio (NPR) is denoted as the ratio of the stagnation chamber pressure to the ambient pressure. The asymmetry originates from the offset in x-coordinates between upper and lower nozzles. To quantitatively analyse this asymmetry, we define a dimensionless form of the extension length of the lower nozzle ($A_1'A_2$ in figure 2) as

$$L_w = \frac{L_{A_1'A_2}}{H_A}. \tag{2.1}$$

When $L_w \neq 0$, expansion waves reflected at the lower jet boundary interact with the slipline first, causing flow deflection downward and resulting in an asymmetric overexpanded jet.

Moreover, it is evident that L_w cannot increase indefinitely. As shown in figure 3(a), when the extension line of the incident shock wave at the upper lip position A_1 intersects precisely with $A_1'A_2$, the asymmetric shock reflection does not exist. Denoting the corresponding L_w as $L_{w,max}$,

$$L_{w,max} = \frac{1}{\tan \beta_{i1}}, \tag{2.2}$$

where β_{i1} is the shock angle of the upper incident shock wave, which can be calculated using the classical oblique shock relations.

Given NPR, ambient pressure and M_0, p_0 can be obtained via the stagnation pressure–static pressure relation for isentropic flow. Then, β_{i1} can be obtained using oblique shock relations. From (2.2), the variation of $L_{w,max}$ with NPR under different Mach numbers is derived, as shown in figure 3(b). Here, $L_{w,max}$ increases with the increase of NPR and decreases with the increase of Mach number.

2.2. *Numerical simulation method*

The boundary conditions are illustrated in figure 4, where AH, BC are set as the wall, AB is set as the pressure inlet, EF is set as the pressure outlet, and CD, DE, FG, GH are set

https://doi.org/10.1017/jfm.2026.11449 Published online by Cambridge University Press

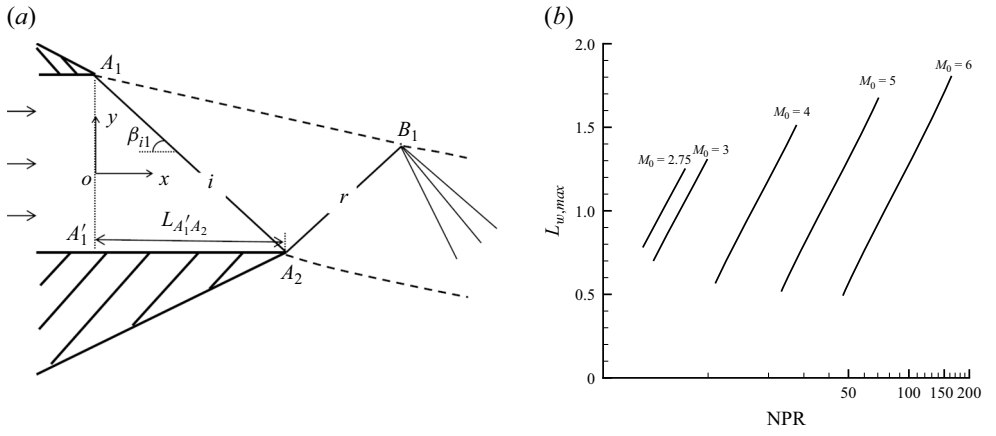


Figure 3. Flow structure and its predictive parameter under $L_{w,max}$. (*a*) Schematic illustration of flow structure corresponding to $L_{w,max}$. (*b*) Variation of the predictive $L_{w,max}$ at different NPR when given M_0.

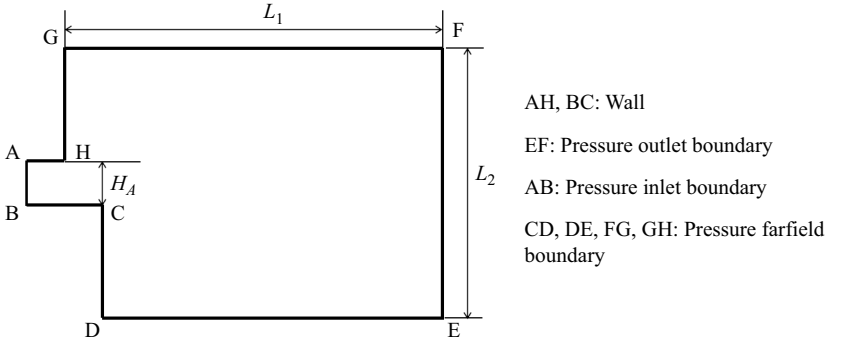


Figure 4. Boundary condition for CFD calculation.

as the pressure far field. To facilitate subsequent verification of the computational domain independence, the dimensions of the computational domain are defined as L_1 and L_2.

We solve the full set of nonlinear Euler equations in gas dynamics using the well-known Roe scheme based on the finite difference approximation and second-order upwinding for the flux. The solution is considered converged when the size and shape of the Mach stem remain unchanged after sufficient iterations. A structured grid is adopted, with refinement applied to regions featuring complex flow structures. It is assumed that the gas flows uniformly from the nozzle in the form of an inviscid ideal gas and the parameters conform to the isentropic flow relationship.

We first conduct domain size independence. Table 1 presents the Mach stem height of different domain size for the condition $M_0 = 3$, $NPR = 7$ and $L_w = 0$. Group A analyses the effects of the computational domain dimensions perpendicular to the flow direction (L_1). When replacing the computational domain size from $10H_A \times 30H_A$ to $10H_A \times 15H_A$, the Mach stem height decreases by only 1.26 %. Group B analyses the effects of the computational domain dimensions along the flow direction (L_2). When changing from $20H_A \times 15H_A$ to $10H_A \times 15H_A$, the increase is merely 1.29 %. Therefore, based on a consideration of accuracy and computational efficiency, L_1 is set as $10H_A$ and L_2 is set as $15H_A$ for subsequent computations.

https://doi.org/10.1017/jfm.2026.11449 Published online by Cambridge University Press

	Computational domain size ($L_1 \times L_2$)	H_m/H_A
Group A	$10H_A \times 5H_A$	0.3874
	$10H_A \times 15H_A$	0.4232
	$10H_A \times 30H_A$	0.4286
	Computational domain size ($L_1 \times L_2$)	H_m/H_A
Group B	$5H_A \times 15H_A$	0.4418
	$10H_A \times 15H_A$	0.4232
	$20H_A \times 15H_A$	0.4178

Table 1. Computational domain size independence test results for $M_0 = 3$, NPR $= 7$, $L_w = 0$.

Grid	N	H_m/H_A
A	80	0.2160
B	150	0.1912
C	300	0.1948

Table 2. Grid configurations and computational domain size independence test results for $M_0 = 3$, NPR $= 9$, $L_w = 0$. N represents the grid number along the Mach stem.

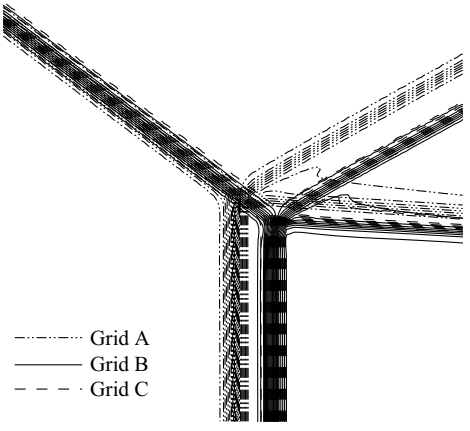


Figure 5. CFD simulation results: Mach number contours of overexpanded jet near the upper triple point under $M_0 = 3$, NPR $= 9$, $L_w = 0$.

Then, we conduct the grid density independence test. Table 2 presents the different grid configurations and corresponding Mach stem height for the condition $M_0 = 3$, $NPR = 9$ and $L_w = 0$. The number of grid nodes distributed along the Mach stem is N. When replacing the grid from Grid C with Grid B, the Mach stem height difference is only 1.85 %. Moreover, figure 5 comparatively displays the Mach number contours near the triple point. The dash–dot–dotted lines, solid lines and dashed lines represent the computational results for Grid A, Grid B and Grid C, respectively. The Mach number contours of Grid B and Grid C are essentially identical. Thus, we conclude that a minimum of 150 grid points must be distributed along the Mach stem to ensure sufficient accuracy of numerical results.

https://doi.org/10.1017/jfm.2026.11449 Published online by Cambridge University Press

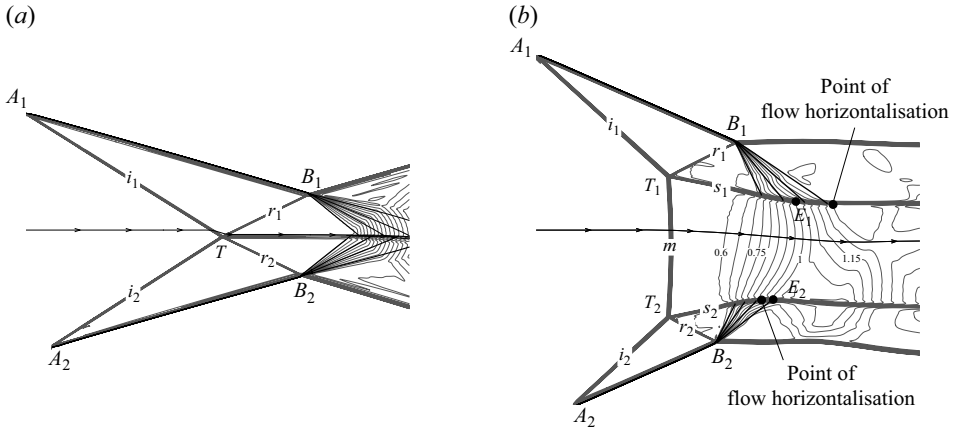


Figure 6. CFD simulation results: Mach number contours (grey solid lines) and characteristic lines (black solid lines) of asymmetric overexpanded jet under $L_w = 0.1$. (*a*) $M_0 = 3$, NPR = 11. (*b*) $M_0 = 3$, NPR = 7.

In summary, the grid used in this study is characterised by a computational domain size of $10H_A \times 15H_A$, with at least 150 grid points guaranteed in the height direction of the Mach stem and a uniformly graded transition adopted in other regions.

2.3. *Analysis of flow structures of asymmetric shock reflection in overexpanded jet*

Figure 6(*a*) shows the CFD results for an asymmetric shock reflection under $M_0 = 3$, NPR = 11, $L_w = 0.1$. The NPR exceeds the von Neumann criterion (von Neumann 1943), resulting in an asymmetric regular reflection. Two incident shocks A_1T and A_2T form at the lip. These two opposite-side incident shocks reflect as two reflected shocks B_1T and B_2T. The reflected shocks interact with the jet boundaries A_1B_1 and A_2B_2, generating two Prandtl–Meyer expansion waves.

Figure 6(*b*) shows the CFD results for an asymmetric shock reflection under $M_0 = 3$, NPR = 7, $L_w = 0.1$. The NPR is in dual solution domain (von Neumann 1943), resulting in an asymmetric Mach reflection. Two incident shocks A_1T_1 and A_2T_2 are connected by a Mach stem T_1T_2. At the triple points T_1 and T_2, two incident shocks reflect as two reflected shocks B_1T_1 and B_2T_2. The region downstream of the Mach stem is initially subsonic and then gradually becomes supersonic, and can be divided into three regions based on whether there is interference from upper/lower reflected expansion waves. Initially, neither the upper nor lower expansion waves interfere with the region downstream of the Mach stem. Subsequently, the lower expansion wave first interferes with the downstream region of the Mach stem. Finally, both the upper and lower expansion waves interfere with the downstream region of the Mach stem. Moreover, the sonic locations E_1 and E_2, and the points of flow horizontalisation are displayed and their positions do not coincide.

3. Theoretical model for asymmetric shock reflection in an overexpanded jet

In this section, a theoretical model for predicting flow field structures in an asymmetric shock reflection in an overexpanded jet is established. The theoretical model aims to describe the shape, position and dimensions of the flow field structures – including the incident shocks, reflected shocks and sliplines for given nozzle exit parameters.

https://doi.org/10.1017/jfm.2026.11449 Published online by Cambridge University Press

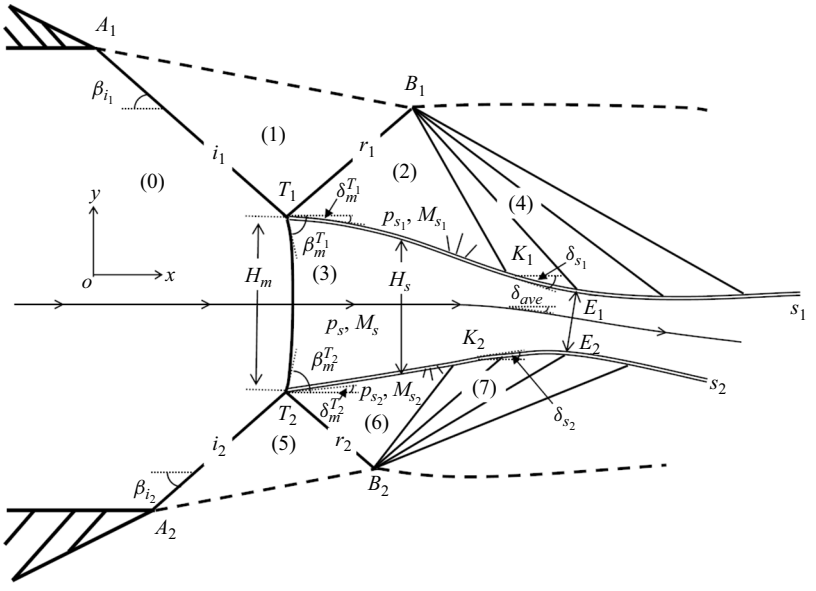


Figure 7. Schematic illustration of asymmetric Mach reflection in an overexpanded jet.

3.1. *Theoretical model of asymmetric shock reflection in an overexpanded jet*

Figure 7 is the schematic illustration of asymmetric Mach reflection in an overexpanded jet. The flow is divided into seven regions: region (0) is upstream of the Mach stem and two incident shock waves; region (1) is between the incident shock wave i_1 and the reflected shock wave r_1; region (2) is between the reflected shock wave r_1 and the expansion wave reflected at point B_1; region (3) is downstream of the Mach stem; region (4) is the region of expansion wave reflected at point B_1; region (5) is between the incident shock wave i_2 and the reflected shock wave r_2; region (6) is between the reflected shock wave r_2 and the expansion wave reflected at point B_2; and region (7) is the region of the expansion wave reflected at point B_2.

Slipline s_1 and slipline s_2 are the upper slipline and lower slipline, respectively. Here, δ_{s_1} and δ_{s_2} are respectively the upper slipline deflection angle and the lower slipline deflection angle, and counterclockwise rotation from the positive x-axis is defined as positive here. There is a noticeable misalignment between the upper and lower interference segments of the sliplines. Therefore, when solving sliplines, the problem should be categorised into three cases: (i) both segments being free; (ii) one segment being free, while the other is an interference segment; and (iii) both segments being interference segments. Here, H_m is the given Mach stem height. The height of the quasi-one-dimensional channel H_s is the height of the quasi-one-dimensional isentropic channel perpendicular to the average flow direction of the throat. Specific expressions are provided in § 3.2.3. Additionally, M_s and p_s are the Mach number and pressure in region (3); M_{s_1} and p_{s_1} are the Mach number and pressure near the upper slipline s_1 in region (2) and region (4); M_{s_2} and p_{s_2} are the Mach number and pressure near the lower slipline s_2 in region (6) and region (7).

3.2. *Analytical methods pertinent to flow field structures*

3.2.1. *Solution of the coordinates of triple points*

The coordinates of triple points should be solved first as the initial coordinates of upper and lower sliplines. As discussed in § 2.3, there is no interaction between the reflected

https://doi.org/10.1017/jfm.2026.11449 Published online by Cambridge University Press

shock wave and the expansion waves reflected at the jet boundary in overexpanded jet shock reflection. The incident shock waves, reflected shock waves and jet boundaries are straight lines, while the Mach stem is an arc with a large radius. Therefore, the geometric relationships for the incident shock waves, reflected shock waves and Mach stem proposed by Lin *et al.* (2019) are used here.

The solution approach of coordinates of triple points is as follows: given the nozzle exit Mach number M_0 and NPR, the classical oblique shock wave relation and triple shock theory (von Neumann 1945) can solve the flow parameters near the triple points. This allows the slopes of the incident shocks to be identified as $-\tan\beta_{i_1}$ and $\tan\beta_{i_2}$, and the deflection angles of the Mach stem near the triple points to be $-\delta_m^{T_1}$ and $\delta_m^{T_2}$. Next, the circular arc hypothesis of the Mach stem is introduced. Tan *et al.* (2006) have discussed the basic assumption that the Mach stem is a circular arc with a large radius, starting from the isentropic small-disturbance equations. Our theoretical model adopts this assumption for the solution. The triple points are assumed to lie on a circle centred at O with radius R. The slopes of OT_1 and OT_2 are $\tan(\pi/2-\beta_m^{T_1})$ and $-\tan(\pi/2-\beta_m^{T_2})$, respectively. With the Mach stem height specified, the coordinates of the triple points T_1 and T_2 can be determined. Subsequently, the coordinates of points B_1 and B_2 can be calculated by solving the straight-line equations of the jet boundary and reflected shock. The detailed equations are shown in Appendix A.

3.2.2. *Governing equations for slipline flow parameters*

Section 2.3 describes the flow field characteristics associated with the free segments of sliplines (T_1K_1 and T_2K_2 in figure 7). Accompanied by the contraction of the one-dimensional isentropic flow region and the resulting pressure drop, secondary expansion waves are generated along the free segment of the slipline to maintain the pressure balance. These secondary waves further influence the slope of the slipline.

This mechanism was applied by Omelchenko *et al.* (2003) to Mach reflection in an overexpanded jet and by Gao & Wu (2010) to that in wedge flows, and was systematically discussed by Silnikov & Chernyshov (2015), who further analysed the possible geometric shapes of the free segment and the interference segment of the slipline. Furthermore, Paramanantham *et al.* (2022) also incorporated this mechanism in their modelling and analysis of shock reflection problems in symmetric jet flows. Furthermore, secondary waves have been accounted for by Bai & Wu (2017) and Paramanantham *et al.* (2022).

Therefore, we can present the governing equations for flow parameters near slipline s_1 in the upper region (2):

$$\begin{cases} \nu\left(M_{s_1}\right)-\nu\left(M_2^{T_1}\right)=-\delta_{s_1}+\delta_m^{T_1}, \\ p_{s_1}=p_2^{T_1}\left(\dfrac{\vartheta\left(M_2^{T_1}\right)}{\vartheta\left(M_{s_1}\right)}\right)^{\dfrac{\gamma}{\gamma-1}}, \end{cases} \tag{3.1}$$

where $M_2^{T_1}$, $p_2^{T_1}$ is the Mach number and pressure of the airflow in region (2) near the triple point T_1; $\nu(M)$ is the Prandtl–Meyer relation and

$$\begin{cases} \vartheta(M)=1+\dfrac{\gamma-1}{2}M^2, \\ \nu(M)=\sqrt{\dfrac{\gamma+1}{\gamma-1}}\arctan\sqrt{\dfrac{\gamma-1}{\gamma+1}(M^2-1)}-\arctan\sqrt{M^2-1}. \end{cases} \tag{3.2}$$

https://doi.org/10.1017/jfm.2026.11449 Published online by Cambridge University Press

Additionally, the governing equations for flow parameters near slipline s_2 in region (6) are

$$\begin{cases} \nu\left(M_{s_2}\right) - \nu\left(M_6^{T_2}\right) = \delta_{s_2} - \delta_m^{T_2}, \\ \\ p_{s_2} = p_6^{T_2}\left(\dfrac{\vartheta\left(M_6^{T_2}\right)}{\vartheta\left(M_{s_2}\right)}\right)^{\dfrac{\gamma}{\gamma-1}}, \end{cases} \tag{3.3}$$

where $M_6^{T_2}$, $p_6^{T_2}$ are the Mach number and pressure of the airflow in region (6) near the triple point T_2.

The flow characteristics of the interference segments of the sliplines (K_1E_1 and K_2E_2 in figure 7) are also described in § 2.3. The pressure drop resulting from the flow passing through the reflected expansion waves is the dominant factor driving the pressure change. To match this pressure drop, the quasi-one-dimensional isentropic flow region contracts, ultimately leading to a change in the curvature of the slipline.

In the solution for a symmetric jet, Paramanantham *et al.* (2022) employed the straight-line assumption to describe the reflected expansion waves and solved for the interference segment of the slipline. In this study, we further assume the reflected expansion waves to be small-curvature curves, based on which the governing equations for flow parameters near the interference segments of the sliplines are established. This assumption aligns with the flow characteristics depicted in figure 6. The derivation of the governing equations for flow parameters in the slipline interference segments can refer to the methodology of Bai (2023), with the distinction that in this model, the expansion waves do not interact with the reflected shock waves.

The expressions for solving the small flow deflection increment $\mathrm{d}\theta_{B_1}$ at position B_1 in region (4) and the angular change $\mathrm{d}\delta_{s_1}$ of slipline s_1 are

$$\begin{cases} \mathrm{d}\theta_{B_1} = \dfrac{L_{21}\Phi_{B_1s_1}\mathrm{d}p_{s_1} + L_{31}}{L_{11} + L_{21}\left(1 + \Phi_{B_1s_1}p_{B_1}\Psi_p\left(M_{B_1}\right)\right)}, \\ \\ \mathrm{d}\delta_{s_1} = \left(1 + \Phi_{B_1s_1}p_{B_1}\Psi_p\left(M_{B_1}\right)\right)\mathrm{d}\theta_{B_1} - \Phi_{B_1s_1}\mathrm{d}p_{s_1}, \end{cases} \tag{3.4}$$

and the expressions for solving the small flow deflection increment $\mathrm{d}\theta_{B_2}$ at position B_2 in region (7) and the angular change $\mathrm{d}\delta_{s_2}$ of slipline s_2 are

$$\begin{cases} \mathrm{d}\theta_{B_2} = \dfrac{L_{22}\Phi_{B_2s_2}\mathrm{d}p_{s_2} + L_{32}}{L_{12} + L_{22}\left(1 + \Phi_{B_2s_2}p_{B_2}\Psi_p\left(M_{B_2}\right)\right)}, \\ \\ \mathrm{d}\delta_{s_2} = \left(1 + \Phi_{B_2s_2}p_{B_2}\Psi_p\left(M_{B_2}\right)\right)\mathrm{d}\theta_{B_2} - \Phi_{B_2s_2}\mathrm{d}p_{s_2}, \end{cases} \tag{3.5}$$

where the $\mathrm{d}x_{s_1}$, $\mathrm{d}y_{s_1}$, $\mathrm{d}x_{s_2}$, $\mathrm{d}y_{s_2}$ are the coordinate increments along the slipline s_1 and s_2, $\mathrm{d}y_{s_1} = -\tan\delta_{s_1}\,\mathrm{d}x_{s_1}$, $\mathrm{d}y_{s_2} = \tan\delta_{s_2}\,\mathrm{d}x_{s_2}$; M_{B_1} and p_{B_1} are the Mach number and pressure in region (4) near B_1; M_{B_2} and p_{B_2} are the Mach number and pressure in region (7) near B_2; θ_{11}, θ_{21} are the angles between the expansion wave and the x-axis at B_1 and near the slipline s_1; θ_{12}, θ_{22} are the angles between the expansion wave and the x-axis at B_2 and near the slipline s_2; for the detailed definitions of L_{11}, L_{21}, L_{31}, $\Phi_{B_1s_1}$, L_{12}, L_{22}, L_{32}, $\Phi_{B_2s_2}$, $\Psi_p(M)$, refer to (B7), (B5), (B7). The detailed mathematical derivations can be found in Appendix B.

Moreover, the Mach number increments near s_1 can be obtained by

$$\mathrm{d}M_{s_1} = \frac{\Psi_M\left(M_{s_1}\right)}{\Psi_p\left(M_{s_1}\right)}\frac{\mathrm{d}p_{s_1}}{p_{s_1}} \tag{3.6}$$

https://doi.org/10.1017/jfm.2026.11449 Published online by Cambridge University Press

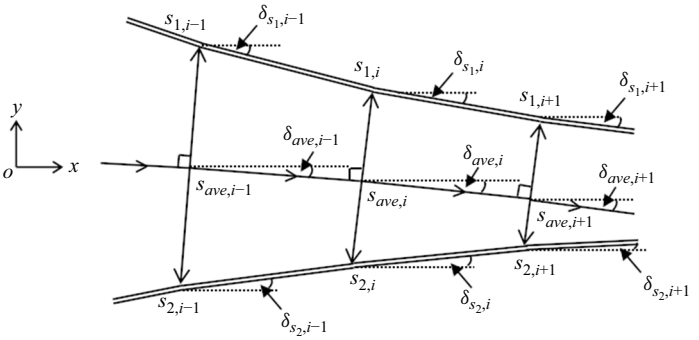


Figure 8. Schematic illustration of sliplines' iterative solution.

and the Mach number increments near s_2 can be obtained by

$$\mathrm{d}M_{s_2} = \frac{\Psi_M\left(M_{s_2}\right)}{\Psi_p\left(M_{s_2}\right)}\frac{\mathrm{d}p_{s_2}}{p_{s_2}}. \tag{3.7}$$

3.2.3. *Iterative solution method and procedure for sliplines*

For the iterative solution of the sliplines, Lin *et al.* (2019) assumed that the average flow deflection angle in region (3) δ_{ave} was equal to the average of the flow deflection angles at triple points T_1 and T_2 of region (3). However, Tao *et al.* (2017) assumed that δ_{ave} continually updates throughout the iteration, equalling the average of the upper/lower slipline angles δ_{s_1} and δ_{s_2}.

The sliplines' iterative solution presented in this study assumes that the value of δ_{ave} remains equal to the average of the upper and lower slipline angles, and continuously updates throughout the iteration process. By integrating the quasi-one-dimensional isentropic flow theory, the pressure equilibrium condition across the slipline and the governing equations for flow parameters near the sliplines, a complete solution for the sliplines is achieved.

Figure 8 is a schematic illustration of the geometric relationship between the upper and lower sliplines from step $i-1$ to step $i+1$ during the iterative solution process. During the advancement, this model assumes that the line segment s_1s_2 is always perpendicular to the mean flow direction.

Taking the case where s_2 first interacts with the expansion wave as an example, the detailed solution steps are as follows.

(i) Given $s_{1,i-1}$ and $s_{2,i-1}$, and the upper/lower slipline angles $\delta_{s_1,i-1}$ and $\delta_{s_2,i-1}$, compute $s_{ave,i}$ and the angle $\delta_{ave,i-1}$:

$$\begin{cases} x_{s_{ave},i} = x_{s_{ave},i-1} + \mathrm{d}x_{ave}, \\ y_{s_{ave},i} = y_{s_{ave},i-1} + \tan\left(\delta_{ave,i-1}\right)\mathrm{d}x_{ave}, \\ \delta_{ave,i-1} = \dfrac{1}{2}\left(\delta_{s_1,i-1} + \delta_{s_2,i-1}\right). \end{cases} \tag{3.8}$$

Additionally, at the start of the slipline advancement and solution process, $x_{s_{ave},1} = 1/2(x_{T_1} + x_{T_2})$, $y_{s_{ave},1} = 1/2(y_{T_1} + y_{T_2})$ and $\delta_{ave} = 1/2(-\delta_m^{T_1} + \delta_m^{T_2})$.

https://doi.org/10.1017/jfm.2026.11449 Published online by Cambridge University Press

(ii) Solve the $s_{2,i}$ and $s_{1,i}$. The equation of the straight $s_{1,i}s_{2,i}$ is

$$y - y_{s_{ave},i} = -\frac{1}{\tan\left(\delta_{ave,i-1}\right)}\left(x - x_{s_{ave},i}\right) \tag{3.9}$$

and the equations of straight $s_{1,i-1}s_{1,i}$, $s_{2,i-1}s_{2,i}$ are

$$\begin{cases} y - y_{s_1,i-1} = -\tan\delta_{s_1,i-1}(x - x_{s_1,i-1}), \\ y - y_{s_2,i-1} = \tan\delta_{s_2,i-1}(x - x_{s_2,i-1}). \end{cases} \tag{3.10}$$

By solving (3.9) and (3.10) simultaneously, the coordinates of $s_{2,i}$ and $s_{1,i}$ can be determined and $\mathrm{d}x_{s_2,i} = x_{s_2,i} - x_{s_2,i-1}$, $\mathrm{d}x_{s_1,i} = x_{s_1,i} - x_{s_1,i-1}$.

(iii) Solve the $H_{s,i}$ and $M_{s,i}$, $p_{s,i}$. Here, $H_{s,i}$ is the height of flow channel and $H_{s,i} = (y_{s_1,i} - y_{s_2,i})/\cos\delta_{ave,i-1}$; $M_{s,i}$ and $p_{s,i}$ follow the quasi-one-dimensional isentropic flow theory relation

$$\begin{cases} \dfrac{H_{s,i}}{H_m} = \dfrac{M_m}{M_{s,i}}\left(\dfrac{\vartheta\left(M_{s,i}\right)}{\vartheta\left(M_m\right)}\right)^{(\gamma+1/2(\gamma-1))}, \\ p_{s,i} = p_m\left(\dfrac{\vartheta\left(M_m\right)}{\vartheta\left(M_{s,i}\right)}\right)^{(\gamma/\gamma-1)}, \end{cases} \tag{3.11}$$

where M_m is the average Mach number and can be expressed as the ratio of the average velocity to the average sonic speed (Li & Ben-Dor 1997*a*,*b*)

$$M_m = \frac{2\left(\rho_3^{T_1}u_3^{T_1}\cos\delta_m^{T_1} + \rho_G u_G\right)}{\left(\rho_3^{T_1} + \rho_G\right)\left(a_3^{T_1} + a_G\right)}, \tag{3.12}$$

where $u_3^{T_1} = a_3^{T_1}M_3^{T_1}$ and $u_G = a_G M_G$; $\rho_3^{T_1}$, $a_3^{T_1}$, $M_3^{T_1}$ are the density, sonic speed and Mach number at region (3) near T_1; ρ_G, a_G M_G can be obtained using the normal shock relations. Here, p_m is the average pressure behind the Mach stem.

(iv) Solve $\delta_{s_1,i}$ and $\delta_{s_2,i}$. Based on the pressure equilibrium relation across the slip lines, it follows that $p_{s_1,i} = p_{s,i} = p_{s_2,i}$ or $\mathrm{d}p_{s_1,i} = (p_{s,i} - p_{s,i-1}) = \mathrm{d}p_{s_2,i}$. The specific solution methods are as follows: when both s_1 and s_2 are in the free segment, $\delta_{s_1,i}$ and $\delta_{s_2,i}$ can be solved using (3.1) and (3.3); when s_2 is in the interference segment and s_1 is in the free segment, $\delta_{s_1,i}$ can be obtained from (3.1), $\mathrm{d}\delta_{s_2,i-1}$ is derived from (3.5) and $\delta_{s_2,i} = \delta_{s_2,i-1} + \mathrm{d}\delta_{s_2,i-1}$; when both s_1 and s_2 are in the interference segment, $\mathrm{d}\delta_{s_1,i-1}$ is derived from (3.4) and $\delta_{s_1,i} = \delta_{s_1,i-1} + \mathrm{d}\delta_{s_1,i-1}$, $\mathrm{d}\delta_{s_2,i-1}$ is derived from (3.5) and $\delta_{s_2,i} = \delta_{s_2,i-1} + \mathrm{d}\delta_{s_2,i-1}$.

(v) Solve $s_{ave,i+1}$, the average flow angle $\delta_{ave,i}$, then repeat steps (i)–(iv) to determine $s_{1,i+1}$, $\delta_{s_1,i+1}$, $s_{2,i+1}$ and $\delta_{s_2,i+1}$.

3.3. *Global solution based on sonic throat compatibility condition*

Bai & Wu (2017) proposed the sonic throat compatibility condition that determines the Mach stem height for classical shock reflection. This condition states that, if the slipline angle is zero $\delta_s = 0$ at the exact location where the sonic throat condition occurs $M_s = M_s^+ = 1$, then this solution is compatible. Lin *et al.* (2019) subsequently refined this criterion by proposing a throat compatibility condition for asymmetric cases, indicating

https://doi.org/10.1017/jfm.2026.11449 Published online by Cambridge University Press

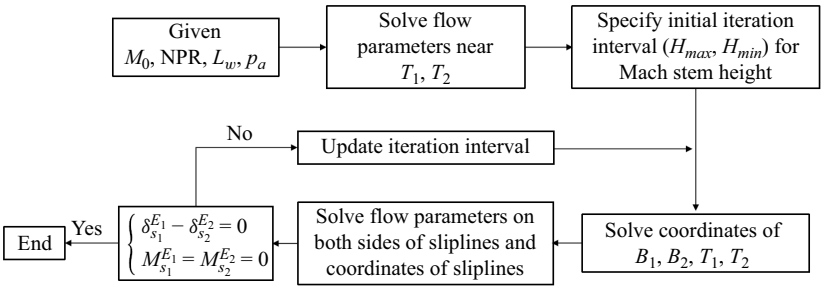


Figure 9. Schematic illustration of global solution flowchart.

that the sonic throat (E_1E_2) locates at the position where the angles of the upper and lower slip lines are equal.

As noted in § 2.3, for an asymmetric overexpanded jet, the sonic throats do not coincide with the points of flow horizontalisation. Therefore, in this work, we adopt the throat compatibility condition given by Lin *et al.* (2019):

$$\begin{cases} \delta_{s_1}^{E_1} - \delta_{s_2}^{E_2} = 0, \\ M_{s_1}^{E_1} = M_{s_2}^{E_2} = 1, \\ \dfrac{y_{E_2} - y_{E_1}}{x_{E_2} - x_{E_1}} = -\dfrac{1}{\tan \delta_{\text{ave}}}, \end{cases} \tag{3.13}$$

which means that at the throat location E_1 and E_2, the Mach number $M_{s_1}^{E_1}$ and $M_{s_2}^{E_2}$ equal 1, and the flow deflection angles of the two sliplines $\delta_{s_1}^{E_1}$ and $\delta_{s_2}^{E_2}$ are equal.

According to the sonic throat compatibility condition for the global model of flow field structures in asymmetric overexpanded jet, the iterative solution flowchart is presented as figure 9, with the specific steps as follows.

(i) Solve the flow parameters near the triple points T_1 and T_2, the triple-shock relation can simply estimate the average values of flow parameters. The pressure, Mach number, temperature near the triple points can be solved, and the shock angles and flow deflection angles of the incident shocks, reflected shocks and jet boundaries can also be obtained.

(ii) According to the nozzle geometry, a solution interval for the Mach stem height is preset as (H_{min}, H_{max}). At the beginning of the solution process, the upper and lower bounds of the solution interval are preset based on the nozzle geometry, as illustrated in figure 10. The initial value of H_{min} is 0 and the initial value of H_{max} is $H_A(1 - L_w \tan \beta_{i_1})$. During the iterative solution process, the Mach stem height solution interval is continuously updated, while the model-predicted Mach stem height remains 0.5 ($H_{min} + H_{max}$).

(iii) Solve the coordinates of triple points T_1 and T_2. Based on the geometric configuration among the incident shock wave, reflected shock wave and Mach stem, the triple point coordinates are determined. Treating the value of H_m obtained from step (ii) as a known quantity, the system yields seven fundamental equations (i.e. (A1)–(A5) in Appendix A) with seven unknowns during the triple point coordinate calculation, thereby admitting a unique solution.

https://doi.org/10.1017/jfm.2026.11449 Published online by Cambridge University Press

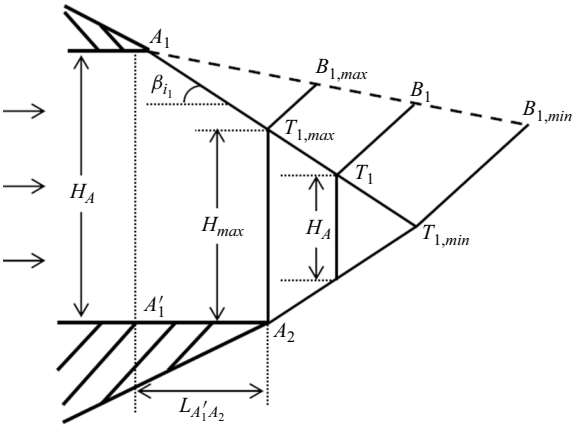


Figure 10. Schematic illustration of initial interval $(0,\ H_A(1 - L_w \tan \beta_{i_1}))$ of Mach stem solution.

(iv) Solve the sliplines. The detailed iterative procedure for solving the sliplines has been provided in § 3.2.3. During the solution process, attention should be paid to identifying the positions of K_1 and K_2 to select the appropriate governing equations.

(v) Update the Mach stem solution interval using the sonic throat compatibility condition. When computing the Mach stem height H_m in step (ii), the shape of the slipline will be uniquely given whether the solution satisfies the sonic throat compatibility condition or not. However, only solutions that meet the sonic throat compatibility conditions are physical. Therefore, during the solution process, the Mach stem solution interval should be continuously updated based on the following conditions until the throat compatibility condition is met. Additionally, the updated conditions are that if $\delta_{s_1}^{E_1} - \delta_{s_2}^{E_2} \neq 0$, $M_{s_1} = M_{s_2} = 1$, then we make $H_{min} = H_m$ and if $\delta_{s_1}^{E_1} - \delta_{s_2}^{E_2} = 0$, $M_{s_1} = M_{s_2} \neq 1$, then we make $H_{max} = H_m$. In this way, steps (i)–(v) are repeated until the solution to the subsonic region corresponding to the accuracy requirement or the height of Mach stem just meets the sonic throat compatibility condition.

4. Theoretical model predictions and analysis

In this section, we analyse the accuracy of the theoretical model in this paper by comparing with previous theoretical models and numerical results under symmetric conditions. By comparing with numerical results, we verified the prediction accuracy of the model under asymmetric conditions. The variation of flow field structure sizes with different nozzle parameters as well as the critical geometric condition for complete misalignment of the interference segment of the upper and lower sliplines is derived.

4.1. *Accuracy of the theoretical model for symmetric Mach reflection in an overexpanded jet*

Figure 11 presents Mach stem height predictions of current model and CFD results, comparing model predictions and numerical results proposed by Paramanantham *et al.* (2022) under different NPR conditions at $M_0 = 2.75$. Significant discrepancies exist between the numerical results of this study and those reported by Paramanantham *et al.* (2022). In their study, Paramanantham *et al.* (2022) performed computations for overexpanded jet shock reflection under symmetric conditions using a 400 × 200

https://doi.org/10.1017/jfm.2026.11449 Published online by Cambridge University Press

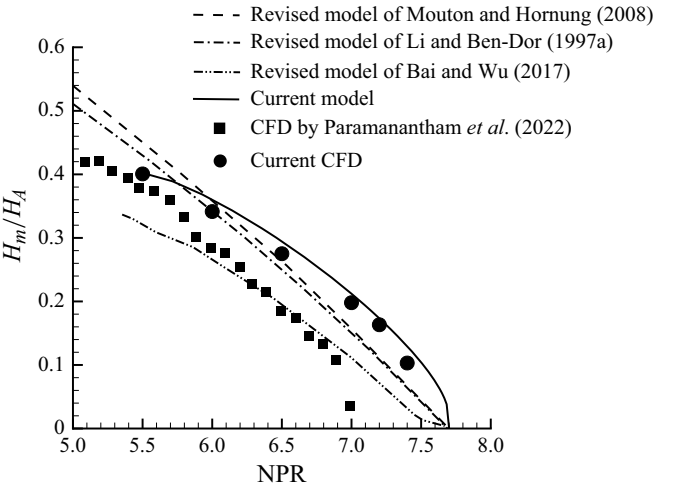


Figure 11. Comparison among current CFD results, current theoretical model results and CFD results, and theoretical model results of Paramanantham *et al.* (2022) under $M_0 = 2.75$.

structured grid within a computational domain of $4H_A \times 2H_A$. Notably, the uniform grid distribution employed proved insufficient for resolving small Mach stems. When the Mach stem height spans a few cells, it becomes easily overlooked. This may explain why their numerical results indicate the disappearance of the Mach stem before reaching the von Neumann point. In contrast, our numerical simulations were conducted on a significantly larger computational domain of $10H_A \times 15H_A$, while maintaining adequate grid resolution along the Mach stem direction. Particularly for cases with higher NPR values (corresponding to smaller Mach stem height), we ensured a minimum of 150 grid points across the Mach stem height to enhance capture accuracy. This enables our numerical calculations to successfully capture the Mach stem at $M_0 = 2.75$ under NPR conditions of 7, 7.2 and 7.4 (prior to reaching the von Neumann point), thereby demonstrating the reliability of our computational approach. Consequently, subsequent comparisons will focus on comparing model predictions with the numerical results from this study. Though all theoretical models accurately predict the NPR corresponding to the von Neumann condition, only our model successfully captures the trend of an increasing slope with NPR and predicts significant Mach stem height even at very low NPR conditions. In general, the Mach stem height predictions from our model demonstrate the best agreement with our numerical results.

A comparison of the CFD results with the predictions of our model is presented in figure 12 under the conditions of $M_0 = 3$ and NPR $= 7$. The predicted Mach stem height deviation (the relative error of the theoretical model with respect to the CFD results) is 3.70 %. Mach number contours obtained by CFD are shown with the solid lines, while the dashed lines depict the model predictions. The predicted triple points and reflected shock waves exhibit a slight upstream shift compared with the CFD results. In general, the incident/reflected shock waves, jet boundaries and sliplines predicted by the current model show good agreement with the CFD results.

Table 3 presents further results of the Mach stem height obtained from the theoretical model and CFD, along with the corresponding deviations, under various nozzle exit conditions. The model-predicted Mach stem height is slightly larger than the CFD results. Maximum deviation of the model-predicted Mach stem height is 4.48 % for $M_0 = 3$. Maximum deviation of the model-predicted Mach stem height is 4.74 % for $M_0 = 4$.

https://doi.org/10.1017/jfm.2026.11449 Published online by Cambridge University Press

Case	M_0	NPR	H_m/H_A (CFD)	H_m/H_A (model)	Deviation (%)
1	3	6.5	0.4564	0.4552	0.26
2	3	7	0.4083	0.4234	3.70
3	3	7.5	0.3726	0.3805	2.12
4	3	8	0.3221	0.3311	2.79
5	3	8.5	0.2634	0.2752	4.48
6	4	14	0.5208	0.5147	1.17
7	4	16	0.4523	0.4714	4.22
8	4	18	0.4013	0.4137	3.09
9	4	20	0.3692	0.3517	4.74
10	4	22	0.2955	0.2849	3.59

Table 3. Comparison of Mach stem height between current model and CFD for symmetric Mach reflection in an overexpanded jet.

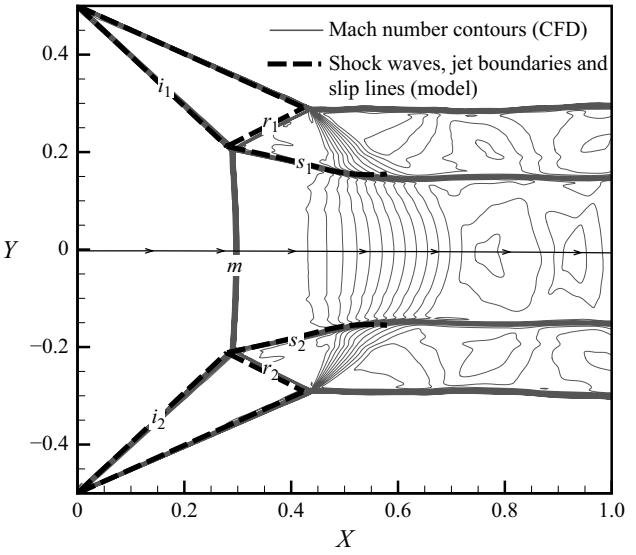


Figure 12. Comparison between current model and CFD under $M_0 = 3$, NPR = 7.

In general, the model demonstrates high accuracy in predicting the Mach stem height for symmetric shock reflection.

Additionally, figure 13 provides further results on the influence of the Mach stem height with nozzle exit parameters as predicted by the model. Figure 13(*a*) shows the influence of Mach stem height with NPR under different M_0 conditions. The Mach stem height decreases as NPR increases and the rate of decrease accelerates with larger NPR. Furthermore, in logarithmic coordinates, as M_0 increases, the curve between NPR and Mach stem height becomes increasingly flat. Figure 13(*b*) shows the influence of Mach stem height with M_0 under different NPR conditions. The Mach stem height increases as M_0 increases and the rate of increase decelerates with larger NPR. Furthermore, under different NPR conditions, the curves between M_0 and Mach stem height are approximately parallel.

In summary, the numerical method employed in this paper provides more accurate capture of flow field structures in symmetric jet Mach reflection. Additionally, our model

https://doi.org/10.1017/jfm.2026.11449 Published online by Cambridge University Press

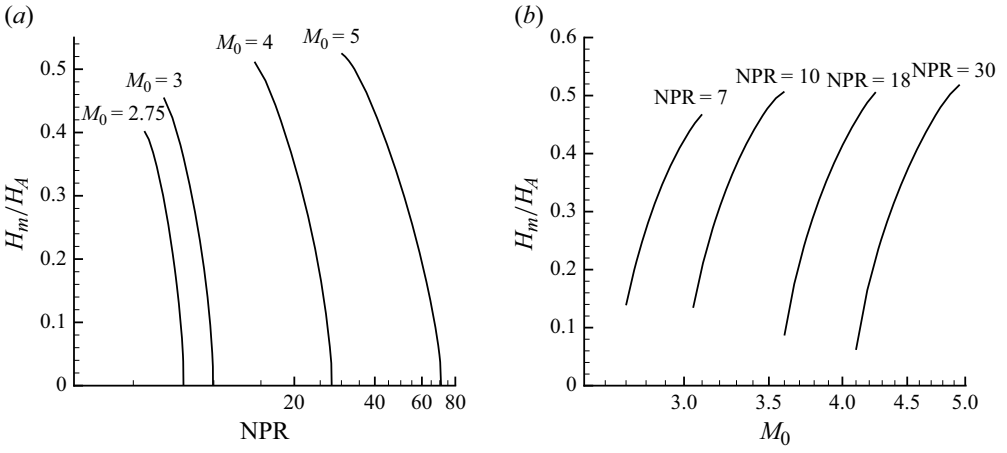


Figure 13. Influence analysis of individual nozzle exit parameters. (*a*) Influence of NPR on Mach stem height under different M_0. (*b*) Influence of M_0 on Mach stem height under different NPR.

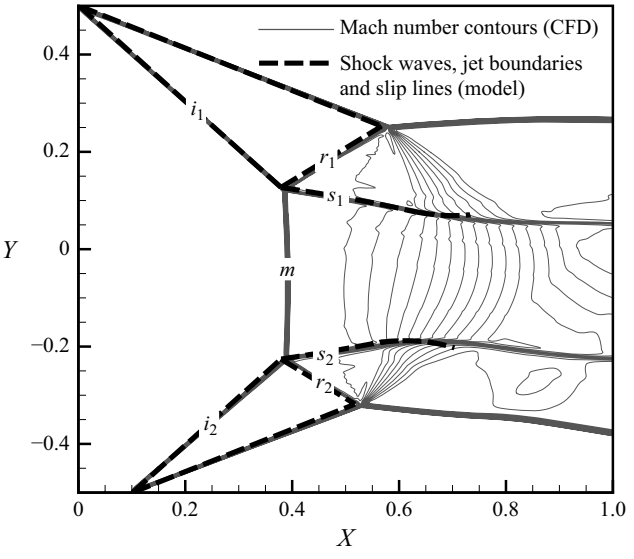


Figure 14. Comparison between current model and CFD under $M_0 = 2.75$, NPR = 6 and $L_W = 0.1$.

demonstrates an excellent predictive capability for the flow field structure. The maximum deviation between model-predicted Mach stem height and numerical results does not exceed 4.74 % for both the $M_0 = 3$ and $M_0 = 4$ cases. Additionally, the Mach stem height decreases as NPR increases and M_0 decreases.

4.2. *Accuracy of the theoretical model for asymmetric Mach reflection in an overexpanded jet*

Figure 14 presents a comparison between the current model and CFD under $M_0 = 2.75$, NPR = 6 and $L_w = 0.1$. The streamline passing through $y = 0$ is depicted. Due to the geometric asymmetry of the nozzle ($L_w = 0.1$), the flow is deflected downward, resulting in streamline deviation towards the lower region. The predicted Mach stem height

https://doi.org/10.1017/jfm.2026.11449 Published online by Cambridge University Press

Case	M_0	NPR	L_w	H_m/H_A (CFD)	H_m/H_A (model)	Deviation (%)
11	3	7	0.05	0.4061	0.4216	3.82
12	3	7	0.1	0.4033	0.4148	2.85
13	3	7	0.15	0.3991	0.4017	0.65
14	3	7	0.2	0.3934	0.3826	2.80
15	4	16	0.05	0.4498	0.4681	4.07
16	4	16	0.1	0.4442	0.4585	3.22
17	4	16	0.15	0.4301	0.4426	2.91
18	4	16	0.19	0.4281	0.4198	1.94

Table 4. Comparison of Mach stem height between current model results and CFD results for an asymmetric jet.

deviation is 2.76 %. The Mach number contour obtained by CFD is shown with the solid lines, while the dashed lines depict the model predictions. The predicted triple points exhibit good agreement compared with the CFD results. In general, the incident/reflected shock waves, jet boundaries and sliplines predicted by the model show good agreement with the CFD results.

Table 4 presents the height of the Mach stem obtained by the current model, CFD and deviations under different nozzle exit conditions. The model-predicted Mach stem height remains slightly larger than the CFD results. Compared with the prediction accuracy for symmetric Mach reflection, the model's accuracy for asymmetric Mach reflection shows a slight decrease. Maximum deviation of the model-predicted Mach stem height does not exceed 3.82 % for $M_0 = 3$ and NPR = 7. The maximum deviation of the model-predicted Mach stem height does not exceed 4.07 % for $M_0 = 4$ and NPR = 16. In general, the model demonstrates high accuracy in predicting the Mach stem height for asymmetric jet flow. Additionally, both CFD and current model results consistently demonstrate that the Mach stem height decreases as L_w increases.

When the M_0 and NPR are given, the triangles $A_1B_1T_1$ and $A_2B_2T_2$ (figure 7) formed by the incident shocks, reflected shocks and jet boundaries above and below are similar. Changing the unilateral L_W actually alters the geometric size of the corresponding triangle. When L_W increases, the lower triangle $A_2B_2T_2$ continuously decreases in size. This change is transmitted to the slipline via expansion waves, altering the geometric shape of the boundary of the subsonic region downstream of the Mach stem (i.e. the slipline). With the nozzle exit flow parameters remaining unchanged, the shock angle does not change; instead, the Mach stem moves in the downstream direction, ultimately resulting in a reduction in its height.

4.3. *Influence of nozzle exit conditions on Mach stem height*

For asymmetric Mach reflection in an overexpanded jet, there is an additional parameter L_w that affects the Mach stem height comparing with the symmetric Mach reflection. Referring to the theoretical formula for the parameters influencing the Mach stem height for symmetric Mach reflection (Paramanantham *et al.* 2022), we can provide the theoretical formula for asymmetric Mach reflection as

$$\frac{H_m}{H_A} = f(M_0, \text{NPR}, L_w, \gamma). \tag{4.1}$$

https://doi.org/10.1017/jfm.2026.11449 Published online by Cambridge University Press

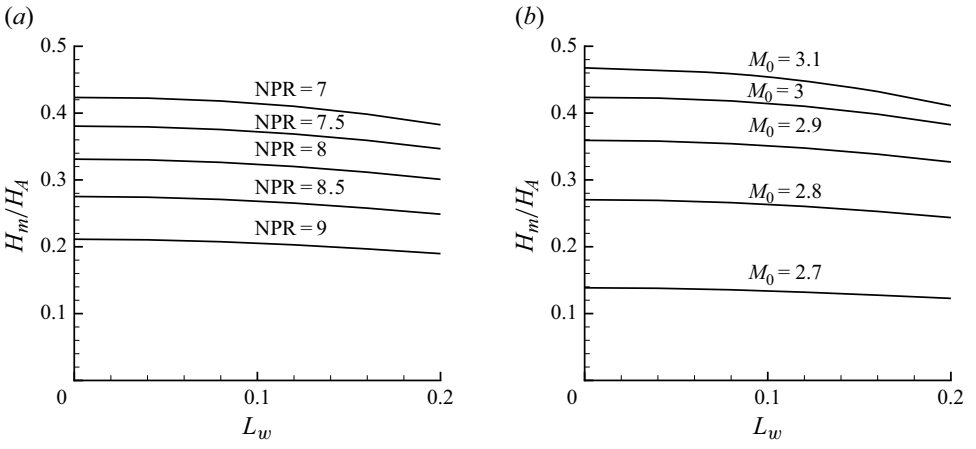


Figure 15. Influence analysis of individual nozzle exit parameters. (*a*) Influence of NPR on Mach stem height with increasing L_w under $M_0 = 3$. (*b*) Influence of M_0 on Mach stem height with increasing L_w under NPR = 7.

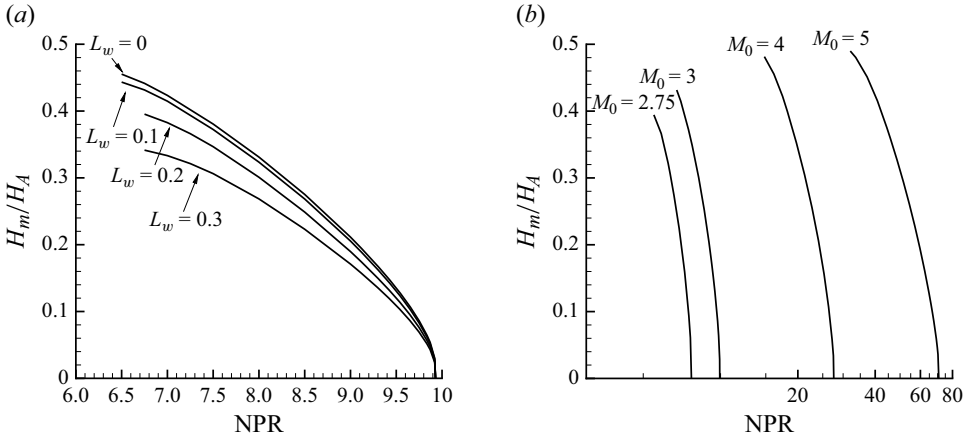


Figure 16. Influence analysis of individual nozzle exit parameters. (*a*) Influence of NPR on the effect of L_w reduction on Mach stem height under $M_0 = 3$. (*b*) Influence of NPR on Mach stem height with different M_0 under $L_w = 0.1$.

Next, we will analyse the effects of several parameters on the Mach stem height. The model-predicted results under different nozzle exit conditions are presented in figures 15, 16 and 17.

Figure 15(*a*) presents the variation of Mach stem height with L_w under different NPR and $M_0 = 3$. Mach stem height slightly decreases as L_W increases. The model predicts that the Mach stem height at $L_w = 0.2$ is 9.64 % lower than that at $L_w = 0$ for NPR = 7. In comparison, the model predicts that the Mach stem height at $L_w = 0.2$ is 10.23 % lower than that at $L_w = 0$ for NPR = 9. This indicates that an increase in NPR enhances the reducing effect of L_w on the Mach stem height.

Figure 15(*b*) presents the variation of Mach stem height with L_w under different M_0 and NPR = 7. The model predicts that the Mach stem height at $L_w = 0.2$ is 12.14 % lower than that at $L_w = 0$ for $M_0 = 3.1$. In comparison, the model predicts that the Mach stem

https://doi.org/10.1017/jfm.2026.11449 Published online by Cambridge University Press

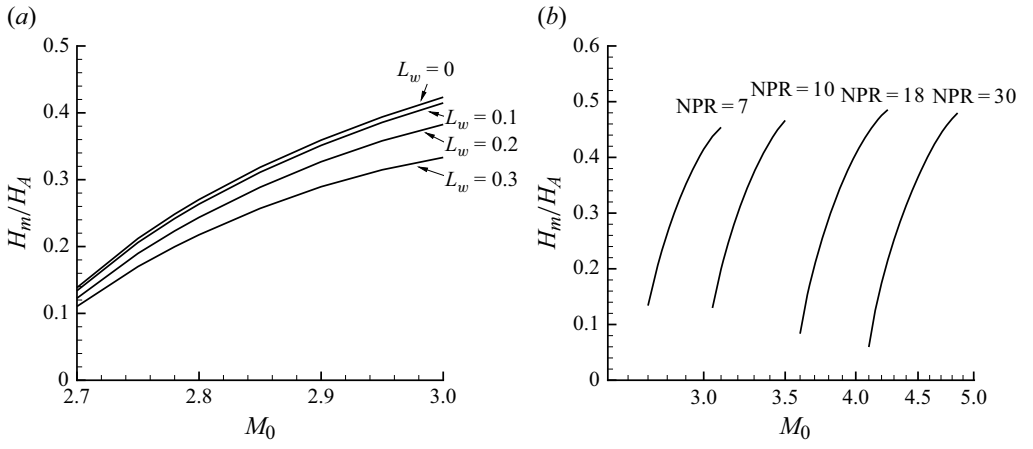


Figure 17. Influence analysis of individual nozzle exit parameters. (*a*) Influence of M_0 on the effect of L_w reduction on Mach stem height under NPR = 7. (*b*) Influence of M_0 on Mach stem height with different NPR under $L_w = 0.1$.

height at $L_w = 0.2$ is 11.42 % lower than that at $L_w = 0$ for $M_0 = 2.7$. This indicates that an increase in M_0 enhances the reducing effect of L_w on the Mach stem height.

Figure 16(*a*) presents the variation of Mach stem height with NPR under different L_w and $M_0 = 3$. The Mach stem height decreases as NPR increases. The model predicts that the Mach stem height at NPR = 9 is 50.08 % lower than that at NPR = 7 for $L_w = 0$. In comparison, the model predicts that the Mach stem height at NPR = 9 is 48.69 % lower than that at NPR = 7 for $L_w = 0.3$. This indicates that an increase in L_w weakens the reducing effect of NPR on the Mach stem height.

Figure 16(*b*) presents the variation of Mach stem height with NPR under different M_0 and $L_w = 0.1$. When compared with the results of the symmetric case ($L_w = 0$) in figure 13(*a*), the curve forms remain largely consistent. Only a slight decrease in Mach stem height is observed, ultimately decreasing to zero at the NPR corresponding to the von Neumann condition.

Figure 17(*a*) presents the variation of Mach stem height with M_0 under different L_w and NPR = 7. The Mach stem height increases as M_0 increases. The model predicts that the Mach stem height at $M_0 = 3$ is 205.55 % higher than that at $M_0 = 2.7$ for $L_w = 0$. In comparison, the model predicts that the Mach stem height at $M_0 = 3$ is 201.80 % higher than that at $M_0 = 2.7$ for $L_w = 0.3$. This indicates that an increase in L_w weakens the enhancement effect of M_0 on the Mach stem height.

Figure 17(*b*) presents the variation of Mach stem height with M_0 under different NPR and $L_w = 0.1$. Similarly, when compared with the symmetric case ($L_w = 0$) results in figure 13(*b*), the curve forms remain largely consistent. Only a slight decrease in Mach stem height is observed and the Mach stem height increases with the Mach number.

In summary, an increase in L_w weakens both the reducing effect of NPR and the enhancement effect of M_0 on the Mach stem height. Furthermore, the reducing effect of L_w is slightly enhanced by the increase in NPR and the increase in M_0.

4.4. *Critical geometric condition for complete misalignment of the interference segment of the upper and lower sliplines*

As L_w gradually increases, the flow field structure will evolve from figure 14 into the form shown in figure 18(*a*), which presents the Mach number contour under $L_w = 0.3$,

https://doi.org/10.1017/jfm.2026.11449 Published online by Cambridge University Press

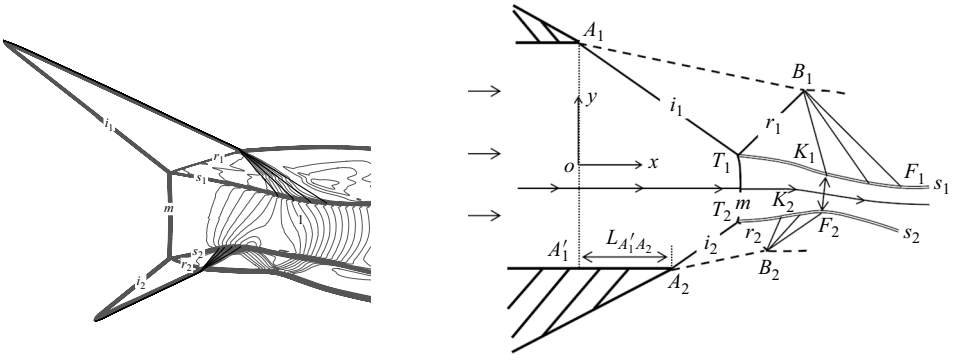


Figure 18. (*a*) Mach number contours (grey solid lines) and characteristic lines (black solid lines) under $M_0 = 4$, NPR = 18, $L_w = 0.3$. (*b*) Schematic illustration of the flow field structures of the complete misalignment of the interference segment of upper/lower sliplines.

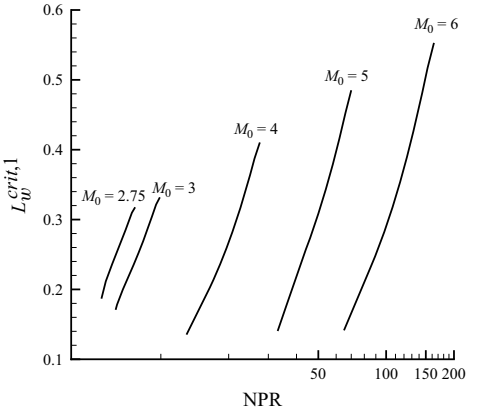


Figure 19. Influence of NPR on L_w^{crit} at different M_0.

$M_0 = 4$ and NPR = 18. It can be observed that the interference segment of upper and lower sliplines become completely misaligned, which means the last expansion wave from one side interacts with the slipline, while the first expansion wave from the opposite side does not interact with the slipline. The Mach number contour line of 1 is marked and the sonic throat location shifts.

A critical flow field structure can be defined, schematically illustrated in figure 18(*b*). This critical state occurs when the last expansion wave generated by the reflected shock on one side (B_2F_2 in figure 18*b*) precisely impinges on the slipline, while the first expansion wave from the opposite reflected shock (B_1K_1 in figure 18*b*) just begins to interact with the slipline. The theoretical model used in this study can be employed to predict L_w for this condition, which is termed L_w^{crit}.

Figure 19 is the prediction of corresponding L_w^{crit} at different NPR when given M_0. For lower nozzle exit Mach numbers ($M_0 = 2.75$ and $M_0 = 3$), the curves show a slight upward convexity. Before the inflection point, L_w^{crit} increases rapidly with NPR; after the inflection point, the growth rate slows down, which indicates that the enhancement effect of the NPR on L_w^{crit} gradually weakens under low-Mach-number conditions. In contrast, for higher Mach numbers ($M_0 = 4$, 5, 6), the curves show a slight concavity downward. Before the inflection point, L_w^{crit} increases slowly with NPR; after the inflection point,

https://doi.org/10.1017/jfm.2026.11449 Published online by Cambridge University Press

the growth rate accelerates, which indicates that the enhancement effect of the NPR on L_w^{crit} gradually intensifies under high-Mach-number conditions. For a given NPR, L_w^{crit} decreases as M_0 increases. At $NPR = 6.5$, L_w^{crit} is 0.26 for $M_0 = 2.75$ and 0.18 for $M_0 = 3$, representing a decrease of 30.77 % when M_0 increases from 2.75 to 3. For a given Mach number, L_w^{crit} increases with increasing NPR. At $M_0 = 4$, L_w^{crit} is 0.14 for NPR = 13 and 0.41 for NPR = 27.5, representing an increase of 192.86 % when NPR increases from 13 to 27.5.

The trend of how L_w^{crit} changes with NPR and M_0 can be easily understood by considering the degree of overexpansion. When other conditions remain constant, decreasing the Mach number or increasing the NPR both lead to a reduction in the intensity of the incident shock wave. In conditions of lower overexpansion (i.e. at lower NPR), the weakened incident shock wave intensity signifies a decrease in the shock wave angle. When the shock wave angle of the incident shock wave decreases, it geometrically results in an increase in the streamwise length of the interaction segments (interference segments) between expansion waves and sliplines. However, increasing L_w actually reduces the length of the lower interference segment and shifts it upstream. When the upper interference segment lengthens, the lower interference segment has more space to move upstream, thereby achieving a larger L_w^{crit}.

5. Concluding remarks

This study focuses on asymmetric shock reflection in a supersonic overexpanded jet induced by nozzle geometric asymmetry, and systematically conducts research through numerical simulations and a theoretical model. The key conclusions are as follows.

(i) Through CFD simulations, we confirm that the flow field structures are highly sensitive to the computational domain and grid density along the Mach stem. Based on independence tests, the computational domain ($10H_A \times 15H_A$) and grid configuration ($\geqslant$150 nodes along the Mach stem) are determined, providing a stable foundation for subsequent theoretical model verification.

(ii) A theoretical model is established and can predict the size and shape of flow field structures (shocks, expansion waves, sliplines). For symmetric shock reflection, the maximum deviation of Mach stem height predicted by the theoretical model is 4.74 % compared with CFD results. For asymmetric shock reflection, the maximum deviation of the Mach stem height predicted by the theoretical model is 4.07 %, demonstrating good consistency with CFD results.

(iii) Influence of nozzle exit conditions on the Mach stem height is studied: the Mach stem height decreases with the increase of NPR and L_w, and decreases as the nozzle exit Mach number (M_0) decreases. Additionally, an increase in L_w weakens both the reducing effect of NPR and the enhancement effect of M_0 on the Mach stem height. The reducing effect of L_w is enhanced by the increase in NPR and the increase in M_0.

(iv) The critical nozzle exit length difference (L_w^{crit}), corresponding to the complete misalignment of the interference segment of upper and lower sliplines, is given. This critical value increases with increasing NPR and decreases with increasing M_0.

This study enriches the theoretical study of asymmetric shock reflection in an overexpanded jet, and the proposed model and obtained laws offer important support for the design of supersonic aircraft engines.

https://doi.org/10.1017/jfm.2026.11449 Published online by Cambridge University Press

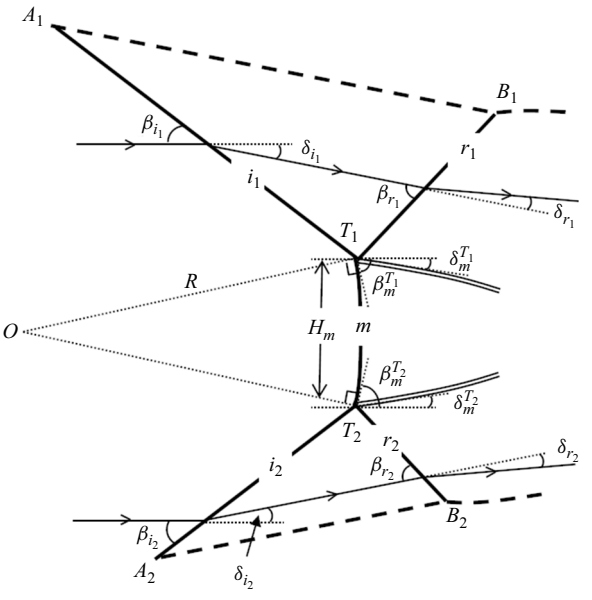


Figure 20. Schematic illustration of geometric relationships among the incident shock waves, reflected shock waves, jet boundaries and Mach stem. Here, i_1 and i_2 represent incident shock waves; r_1 and r_2 represent reflected shock waves.

Acknowledgements. The authors are grateful to all referees for their useful comments and references, which helped improve the manuscript.

Funding. The authors appreciate the financial support from Tianmushan Laboratory (Grant No. TK-2024-D-004), the National Natural Science Foundation of China (Nos. 12472232 and 52192632), and the Beihang University Young Elite Talent Support Program (No. 501XYGG2025105003).

Declaration of interests. The authors report no conflict of interest.

Appendix A. Geometric relations and three shock-wave theory for solving triple points

Here, we will discuss the geometric relationships that will be used to solve the incident shock waves, reflected shock waves, jet boundaries and Mach stem when the Mach stem height H_m is determined. Figure 20 is a schematic illustration of geometric relationships among the incident shock waves, reflected shock waves, jet boundaries and Mach stem. Here, H_A represents the nozzle diameter and we have the coordinates of A_1 and A_2.

$$\begin{cases} x_{A_1} = 0, \\ x_{A_2} = L_w, \\ y_{A_{1,2}} = \pm\dfrac{1}{2}H_A, \end{cases} \tag{A1}$$

where the definition of L_w is provided in § 2.1. By taking flow structures located in the upper half of the x-axis as an example, the equations for the incident shock A_1T_1 can be confirmed:

$$y - y_{A_1} = -\tan\left(\beta_{i_1}\right)\left(x - x_{A_1}\right) \tag{A2}$$

https://doi.org/10.1017/jfm.2026.11449 Published online by Cambridge University Press

and the jet boundary A_1B_1 is

$$y - y_{A_1} = -\tan\left(\delta_{i_1}\right)\left(x - x_{A_1}\right), \tag{A3}$$

where β_{i_1} is the shock angle of upper incident shock and δ_{i_1} is equal to the flow deflection angle of the upper incident shock. The solution of incident shock i_2 and jet boundary A_2T_2 follow the same rule.

Then, Lin *et al.* (2019) used the circular arc assumption for the Mach stem, and successfully solved the flow structures for classical asymmetric shock reflection problems. Here, the same assumption is adopted to solve the coordinate of the triple points. As shown in figure 7, the triple points, T_1, T_2, lie on the Mach stem and incident shock waves (i_1 and i_2), which means that the following geometrical relations hold:

$$\begin{cases} y_{T_1} - y_{A_1} = -\tan\left(\beta_{i_1}\right)\left(x_{T_1} - x_{A_1}\right), \\ y_{T_2} - y_{A_2} = \tan\left(\beta_{i_2}\right)\left(x_{T_2} - x_{A_2}\right), \\ \left(x_{T_1} - x_O\right)^2 + \left(y_{T_1} - y_O\right)^2 = R^2, \\ \left(x_{T_2} - x_O\right)^2 + \left(y_{T_2} - y_O\right)^2 = R^2, \end{cases} \tag{A4}$$

where β_{i_2} is the shock angle of lower incident shock, O is the centre of the circle where the Mach stem is located and R is the radius of the circle. The assumption also gives the tangential relations between incident shock (i_1 and i_2) and Mach stem (T_1T_2). The slopes of Mach stem at the triple points can be obtained by using the circular shape relation. Additionally, these slopes are equal to the tangent of shock angles $\beta_m^{T_1}$ and $\beta_m^{T_2}$. By giving the Mach stem length H_m in advance, we have

$$\begin{cases} \left(x_{T_1} - x_{T_2}\right)^2 + \left(y_{T_1} - y_{T_2}\right)^2 = H_m^2, \\ \dfrac{y_{T_1} - y_O}{x_{T_1} - x_O} = \dfrac{1}{\tan\left(\beta_m^{T_1}\right)}, \\ \dfrac{y_{T_2} - y_O}{x_{T_2} - x_O} = -\dfrac{1}{\tan\left(\beta_m^{T_2}\right)}. \end{cases} \tag{A5}$$

The tangent of shock angles β_{i_1}, β_{i_2}, $\beta_m^{T_1}$ and $\beta_m^{T_2}$, and the flow deflection angle δ_{i_1} can be obtained by using the classical oblique shock wave relations and the three-shock theory (von Neumann 1945).

There are seven unknown parameters, and seven equations in (A4) and (A5), so we can uniquely solve the unknowns x_{T_1}, x_{T_2}, y_{T_1}, y_{T_2}, x_O, y_O, R. Then, the equation for the straight line of the reflected shock can be established. Here, the upper reflected shock is again taken as an example:

$$y - y_{T_1} = \tan\left(\beta_{r_1} - \delta_{i_1}\right)\left(x - x_{T_1}\right), \tag{A6}$$

where β_{r_1} is the shock angle of upper reflected shock. By solving (A2) and (A6) simultaneously, the coordinates of points B_1 can be determined. The solution of B_2 follows the same rule.

Appendix B. Solution for the interference segments of sliplines

Here, we take the lower slipline s_2 interference segment as an example to derive the governing equations of flow parameters. For the expansion waves in region (7), their

https://doi.org/10.1017/jfm.2026.11449 Published online by Cambridge University Press

geometric morphology satisfies the following differential form of the curve equation:

$$\mathrm{d}y_{s_2} - \tan \Lambda_2 \, \mathrm{d}x_{s_2} = \left(x_{s_2} - x_{B_2}\right)\left(\Lambda_{\theta_{12}} \, \mathrm{d}\theta_{12} + \Lambda_{\theta_{22}} \, \mathrm{d}\theta_{22}\right) \cos^{-2} \Lambda_2, \tag{B1}$$

where the $\mathrm{d}y_{s_2}$ and $\mathrm{d}x_{s_2}$ are the coordinate increments along the slipline s_2 and $\mathrm{d}y_{s_2} = \tan \delta_{s_2} \mathrm{d}x_{s_2}$; x_{B_2} is the x-coordinate of B_2; $\theta_{12} = \theta_{B_2} + \mu_{B_2}$, $\theta_{22} = \theta_{s_2} + \mu_{s_2}$ are the angles between the expansion wave and the x-axis at B_2 and near the slipline s_2, respectively. Additionally, we have

$$\begin{cases} \Lambda_2(\theta_{12}, \theta_{22}) = \arctan \dfrac{2 \tan \theta_{12} + \tan(\theta_{22} - \theta_{12})}{2 - \tan \theta_{12} \tan(\theta_{22} - \theta_{12})}, \\ \Lambda_{\theta_{12}}(\theta_{12}, \theta_{22}) = -\dfrac{\tan^2(\theta_{12} - \theta_{22}) - 2}{\tan^2(\theta_{12} - \theta_{22}) + 4}, \\ \Lambda_{\theta_{22}}(\theta_{12}, \theta_{22}) = \dfrac{2 \tan^2(\theta_{12} - \theta_{22}) + 2}{\tan^2(\theta_{12} - \theta_{22}) + 4}. \end{cases} \tag{B2}$$

By taking the differentials of θ_{12} and θ_{22}, we can have $\mathrm{d}\theta_{12} = \mathrm{d}\theta_{B_2} + \mathrm{d}\mu_{B_2} = (1 + (\mathrm{d}\mu_{B_2}/\mathrm{d}\theta_{B_2}))\, \mathrm{d}\theta_{B_2}$ and $\mathrm{d}\theta_{22} = \mathrm{d}\theta_{s_2} + \mathrm{d}\mu_{s_2}$. For $\mathrm{d}\theta_{12}$, we introduce the relationship between the Mach angle and the flow deflection angle under a small deflection increment $\mathrm{d}\theta_{B_2}$ within the expansion wave. For $\mathrm{d}\theta_{22}$, we further incorporate the relationship between the Mach angle and the Mach number, along with the compatibility condition valid along the streamline (characteristic line C_0). Ultimately, the following expression is obtained:

$$\begin{cases} \mathrm{d}\theta_{12} = \left(1 + \Psi_\mu\left(M_{B_2}\right)\right) \mathrm{d}\theta_{B_2}, \\ \mathrm{d}\theta_{22} = \mathrm{d}\delta_{s_2} + \dfrac{\Omega_M\left(M_{s_2}\right)\Psi_M\left(M_{s_2}\right)}{\Psi_p\left(M_{s_2}\right)} \dfrac{\mathrm{d}p_{s_2}}{p_{s_2}}, \end{cases} \tag{B3}$$

where

$$\begin{cases} \Psi_\mu(M) = \dfrac{\vartheta(M)}{M^2 - 1}, \\ \Omega_M(M) = -\dfrac{1}{M\sqrt{M^2 - 1}}, \\ \Psi_M(M) = -\dfrac{M\vartheta(M)}{\sqrt{M^2 - 1}}. \end{cases} \tag{B4}$$

Subsequently, we supplement the differential form of the compatibility relation valid along the characteristic line (C_-),

$$\begin{cases} \mathrm{d}\theta_{B_2} - \mathrm{d}\delta_{s_2} = \Phi_{B_2 s_2}\left(\mathrm{d}p_{s_2} - \mathrm{d}p_{B_2}\right), \\ \Phi_{B_2 s_2} = \dfrac{1}{2}\left(\Phi_{B_2} + \Phi_{s_2}\right), \ \Phi(p, M) = \dfrac{\sqrt{M^2 - 1}}{\gamma M^2 p}. \end{cases} \tag{B5}$$

By supplementing the relationship between pressure and flow deflection angle under a small deflection increment, we get

$$\mathrm{d}p_{B_2} = p_{B_2} \Psi_p\left(M_{B_2}\right) \mathrm{d}\theta_{B_2}. \tag{B6}$$

https://doi.org/10.1017/jfm.2026.11449 Published online by Cambridge University Press

Finally, substituting (B2) into (B1) and combining with (B5), we obtain expressions for solving $\mathrm{d}\theta_{B_2}$ and $\mathrm{d}\delta_{s_2}$,

$$\begin{cases} \mathrm{d}\theta_{B_2} = \dfrac{L_{22}\Phi_{B_2s_2}\,\mathrm{d}p_{s_2} + L_{32}}{L_{12} + L_{22}\left(1 + \Phi_{B_2s_2}p_{B_2}\Psi_p\left(M_{B_2}\right)\right)}, \\ \mathrm{d}\delta_{s_2} = \left(1 + \Phi_{B_2s_2}p_{B_2}\Psi_p\left(M_{B_2}\right)\right)\mathrm{d}\theta_{B_2} - \Phi_{B_2s_2}\,\mathrm{d}p_{s_2}, \\ L_{12} = \left(x_{s_2} - x_{B_2}\right)\Lambda_{\theta_{12}}\cos^{-2}\Lambda_2\left(1 + \Psi_\mu\left(M_{B_2}\right)\right), \\ L_{22} = \left(x_{s_2} - x_{B_2}\right)\Lambda_{\theta_{22}}\cos^{-2}\Lambda_2, \\ L_{32} = \left(\tan\delta_{s_2} - \tan\Lambda_2\right)\mathrm{d}x_{s_2} - \left(x_{s_2} - x_{B_2}\right)\Lambda_{\theta_{22}}\cos^{-2}\Lambda_2\dfrac{\Omega_M\left(M_{s_2}\right)\Psi_M\left(M_{s_2}\right)}{\Psi_p\left(M_{s_2}\right)}\dfrac{\mathrm{d}p_{s_2}}{p_{s_2}}. \end{cases} \tag{B7}$$

The process of solving for $\mathrm{d}\theta_{B_1}$ and $\mathrm{d}\delta_{s_1}$ is similar, and only the final results are presented here:

$$\begin{cases} \mathrm{d}\theta_{B_1} = \dfrac{L_{21}\Phi_{B_1s_1}\mathrm{d}p_{s_1} + L_{31}}{L_{11} + L_{21}\left(1 + \Phi_{B_1s_1}p_{B_1}\Psi_p\left(M_{B_1}\right)\right)}, \\ \mathrm{d}\delta_{s_1} = \left(1 + \Phi_{B_1s_1}p_{B_1}\Psi_p\left(M_{B_1}\right)\right)\mathrm{d}\theta_{B_1} - \Phi_{B_1s_1}\,\mathrm{d}p_{s_1}, \\ L_{11} = -\left(x_{s_1} - x_{B_1}\right)\Lambda_{\theta_{11}}\cos^{-2}\Lambda_1\left(1 + \Psi_\mu\left(M_{B_1}\right)\right), \\ L_{21} = -\left(x_{s_1} - x_{B_1}\right)\Lambda_{\theta_{21}}\cos^{-2}\Lambda_1, \\ L_{31} = \left(-\tan\delta_{s_1} - \tan\Lambda_1\right)\mathrm{d}x_{s_1} + \left(x_{s_1} - x_{B_1}\right)\Lambda_{\theta_{21}}\cos^{-2}\Lambda_1\dfrac{\Omega_M\left(M_{s_1}\right)\Psi_M\left(M_{s_1}\right)}{\Psi_p\left(M_{s_1}\right)}\dfrac{\mathrm{d}p_{s_1}}{p_{s_1}}, \end{cases} \tag{B8}$$

where $\mathrm{d}y_{s_1}$ and $\mathrm{d}x_{s_1}$ are the coordinate increments along the slipline s_1 and $\mathrm{d}y_{s_1} = -\tan\delta_{s_1}\mathrm{d}x_{s_1}$. Additionally, we have

$$\begin{cases} \Lambda_1(\theta_{11}, \theta_{21}) = \arctan\dfrac{2\tan\theta_{11} + \tan(\theta_{21} - \theta_{11})}{2 - \tan\theta_{11}\tan(\theta_{21} - \theta_{11})}, \\ \Lambda_{\theta_{11}}(\theta_{11}, \theta_{21}) = -\dfrac{\tan^2(\theta_{11} - \theta_{21}) - 2}{\tan^2(\theta_{11} - \theta_{21}) + 4}, \\ \Lambda_{\theta_{21}}(\theta_{11}, \theta_{21}) = \dfrac{2\tan^2(\theta_{11} - \theta_{21}) + 2}{\tan^2(\theta_{11} - \theta_{21}) + 4}, \\ \Phi_{B_1s_1} = \dfrac{1}{2}\left(\Phi_{B_1} + \Phi_{s_1}\right), \end{cases} \tag{B9}$$

where x_{B_1} is the x-coordinate of B_1, and $\theta_{11} = -(\theta_{B_1} + \mu_{B_1})$, $\theta_{21} = -(\theta_{s_1} + \mu_{s_1})$ are the angles between the expansion wave and the x-axis at B_1 and near the slipline s_1, respectively.

https://doi.org/10.1017/jfm.2026.11449 Published online by Cambridge University Press

References

Arun Kumar, R. & Rajesh, G. 2017 Shock transformation and hysteresis in underexpanded confined jets. *J. Fluid Mech.* **823**, 538–561.

Ashratov, E.A. 1966 Calculations of axisymmetric jet leaving a nozzle at jet pressure lower than pressure in medium. *Fluid Dyn.* **1** (1), 113–115.

Azevedo, D.J. & Liu, C.S. 1993 Engineering approach to the prediction of shock patterns in bounded high-speed flows. *AIAA J.* **31** (1), 83–90.

Bai, C.-Y. 2023 Shock reflection with incident shock–wedge trailing-edge expansion fan interaction. *J. Fluid Mech.* **968**, A21.

Bai, C.-Y. 2024 Reflection of a centred compression wave. *J. Fluid Mech.* **984**, A3.

Bai, C.-Y. & Wu, Z.-N. 2017 Size and shape of shock waves and slipline for Mach reflection in steady flow. *J. Fluid Mech.* **818**, 116–140.

Bai, C.-Y. & Wu, Z.-N. 2021 A study of the dependence of the Mach stem height on the trailing edge height. *Fluids* **6** (9), 313.

Ben-Dor, G., Dewey, J.M. & Takayama, K. 1987 The reflection of a plane shock wave over a double wedge. *J. Fluid Mech.* **176**, 483–520.

Ben-Dor, G., Ivanov, M., Vasilev, E.I. & Elperin, T. 2002 Hysteresis processes in the regular reflection to Mach reflection transition in steady flows. *Prog. Aerosp. Sci.* **38** (4), 347–387.

Chernyshov, M.V., Savelova, K.E. & Kapralova, A.S. 2021 Approximate analytical models of shock-wave structure at steady Mach reflection. *Fluids* **6** (9), 305.

Chow, W.L. & Chang, I.S. 1975 Mach reflection associated with over-expanded nozzle free jet flows. *AIAA J.* **13** (6), 762–766.

Gao, B. & Wu, Z.N. 2010 A study of the flow structure for Mach reflection in steady supersonic flow. *J. Fluid Mech.* **656**, 29–50.

Guan, X.-K., Bai, C.-Y., Lin, J. & Wu, Z.-N. 2020 Mach reflection promoted by an upstream shock wave. *J. Fluid Mech.* **903**, A44.

Guan, X.-K., Bai, C.-Y. & Wu, Z.-N. 2018 Steady Mach reflection with two incident shock waves. *J. Fluid Mech.* **855**, 882–909.

Hadjadj, A., Kudryavtsev, A.N. & Ivanov, M.S. 2004 Numerical investigation of shock-reflection phenomena in overexpanded supersonic jets. *AIAA J.* **42** (3), 570–577.

Henderson, L.F. & Lozzi, A. 1975 Experiments on transition of Mach reflexion. *J. Fluid Mech.* **68** (1), 139–155.

Hew, J.K.J., Boswell, R.W., Federrath, C., Gopalapillai, R. & Paramanantham, V. 2023 Analytical and numerical studies of the non-uniformity induced type II asymmetric cap shock Mach reflection in over-expanded supersonic jets.

Hew, J.K.J., Ogawa, H. & Boswell, R.W. 2024 Centerline shock reflection for supersonic internal flows in the non-Rankine–Hugoniot zone: overexpanded supersonic microjets. *Phys. Fluids* **36** (9), 091709.

Hornung, H.G., Oertel, H. & Sandeman, R.J. 1979 Transition to Mach reflexion of shock waves in steady and pseudosteady flow with and without relaxation. *J. Fluid Mech.* **90** (3), 541–560.

Huang, W., Wu, H., Yang, Y.-G., Yan, L., Li, S.-B. 2020 Recent advances in the shock wave/boundary layer interaction and its control in internal and external flows. *Acta Astronaut.* **174**, 103–122.

Häberle, J. & Gülhan, A. 2007 Internal flowfield investigation of a hypersonic inlet at Mach 6 with bleed. *J. Propul. Power* **23** (5), 1007–1017.

Ivanov, M.S., Vandromme, D., Fomin, V.M., Kudryavtsev, A.N., Hadjadj, A. & Khotyanovsky, D.V. 2001 Transition between regular and Mach reflection of shock waves: new numerical and experimental results. *Shock Waves* **11** (3), 199–207.

Ji, J., Li, Z., Zhang, E. & Yang, J. 2019 Shock interactions in near-axisymmetric internal contraction flows. *J. Exp. Fluid Mech.* **33** (5), 1–9.

Kashitani, M., Yamaguchi, Y., Miyazato, Y., Masuda, M. & Matsuo, K. 2003 Configuration of shock waves in two-dimensional overexpanded jets. *J. Therm. Sci.* **12** (4), 294–298.

Lavala, S.R. & Das, S. 2025 Flow field and acoustic studies on a supersonic jet with tabs having various cross sections. *J. Aerospace Eng.* **38** (1), 04024104.

Li, Z.-D. & Bai, C.-Y. 2025 Reflection of multiple incident shock waves and shock interaction train. *J. Fluid Mech.* **1008**, A28.

Li, H. & Ben-Dor, G. 1997*a* A parametric study of Mach reflection in steady flows. *J. Fluid Mech.* **341**, 101–125.

Li, H. & Ben-Dor, G. 1997*b* Mach reflection wave configuration in two-dimensional supersonic jets of overexpanded nozzles. *AIAA J.* **36** (3), 488–491.

https://doi.org/10.1017/jfm.2026.11449 Published online by Cambridge University Press

LI, X., HE, F., ZHANG, X., HAO, P., WU, X. & LIU, N. 2024 Experimental study on acoustic resonance of subsonic and slightly underexpanded impinging jets. *J. Fluid Mech.* **983**, A32.

LIN, J., BAI, C.-Y. & WU, Z.-N. 2019 Study of asymmetrical shock wave reflection in steady supersonic flow. *J. Fluid Mech.* **864**, 848–875.

LV, Z., XU, J., YU, Y. & MO, J. 2017 A new design method of single expansion ramp nozzles under geometric constraints for scramjets. *Aerosp. Sci. Technol.* **66**, 129–139.

MACH, E. 1878 Uber den verlauf von funkenwellen in der ebene und im raume. *Sitzungsbr. Akad. Wiss. Wien* **78**, 819–838.

MATSUO, S., SETOGUCHI, T., NAGAO, J., ALAM, M.M.A. & KIM, H.D. 2011 Experimental study on hysteresis phenomena of shock wave structure in an over-expanded axisymmetric jet. *J. Mech. Sci. Technol.* **25** (10), 2559–2565.

MENG, B.Q., HAN, G.L., YUAN, C.K., WANG, C. & JIANG, Z.L. 2017 Experimental and numerical study on hypersonic flow over double-wedge configuration. *AIAA J.* **55** (9), 3227–3230.

MOUTON, C.A. & HORNUNG, H.G. 2007 Mach stem height and growth rate predictions. *AIAA J.* **45** (8), 1977–1987.

OMELCHENKO, A., USKOV, V. & CHERNYSHOV, M.V. 2003 An approximate analytical model of flow in the first barrel of an overexpanded jet. *Tech. Phys. Lett.* **29**, 243–245.

ONOFRI, M. & NASUTI, F. 1999 The physical origins of side loads in rocket nozzles. In *35th Joint Propulsion Conference and Exhibit*. American Institute of Aeronautics and Astronautics.

PARAMANANTHAM, V., JANAKIRAM, S. & GOPALAPILLAI, R. 2022 Prediction of Mach stem height in compressible open jets. Part 1. Overexpanded jets. *J. Fluid Mech.* **942**, A48.

POWELL, A. 1953 On the mechanism of choked jet noise. *Proc. Phys. Soc. Sect. B* **66** (12), 1039.

QIN, Z., SHI, A., DOWELL, E.H., PEI, Y. & HUANG, E. 2022 Analytical model of strong Mach reflection. *AIAA J.* **60** (9), 5187–5202.

ROLLAND, V., SHOESMITH, B. & TIMOFEEV, E. 2024 A semi-analytical model for Mach reflection in axisymmetric overexpanded jets. In *AIAA SCITECH 2024 Forum*. American Institute of Aeronautics and Astronautics.

ROY, S. & GOPALAPILLAI, R. 2019 An analytical model for asymmetric Mach reflection configuration in steady flows. *J. Fluid Mech.* **863**, 242–268.

ROY, S. & RAJESH, G. 2017 Analytical prediction of Mach stem height for asymmetric wedge reflection in 2-d steady flows. In *31st International Symposium on Shock Waves*, vol. 1, pp. 855–863.

SHI, C., YOU, Y., ZHENG, X. & ZHU, C. 2023 Analytical model for curved-shock Mach reflection. *Phys. Fluids* **35** (3), 031702.

SHIMSHI, E., BEN-DOR, G. & LEVY, A. 2009 Viscous simulation of shock-reflection hysteresis in overexpanded planar nozzles. *J. Fluid Mech.* **635**, 189–206.

SHIMSHI, E., BEN-DOR, G. & LEVY, A. 2015 On the transition from regular to Mach reflection in overexpanded planar jets. In *29th International Symposium on Shock Waves 2* (ed. R. Bonazza & D. Ranjan), p. 1385.

SHOESMITH, B. & TIMOFEEV, E. 2025 Shock reflection from an axial cylinder in axisymmetric supersonic steady flow. *Shock Waves*. **35**, 759–771.

SILNIKOV, M.V. & CHERNYSHOV, M.V. 2015 The interaction of a Prandtl–Meyer wave and a quasi-one-dimensional flow region. *Acta Astronaut.* **109**, 248–253.

SUN, H., ZHANG, J., MA, X. & XUE, R. 2024 Shock wave control for supersonic inlet with high-frequency pulsed arc discharge plasma. *AIAA J.* **62** (12), 4888–4892.

TAN, L.H., REN, Y.X. & WU, Z.N. 2006 Analytical and numerical study of the near flow field and shape of the Mach stem in steady flows. *J. Fluid Mech.* **546**, 341–362.

TANG, X.B., CAI, J., HUANG, H.X., TAN, H.J., QIN, Y. & TIAN, Y. 2025*a* On the centered-compression waves/cowl shock interaction from opposite-family in hypersonic inlet with inward deflection cowl: an inviscid perspective. *Phys. Fluids* **37** (7), 076153.

TANG, X.-B., CAI, J., LIU, Z.-J., HUANG, H.-X., QIN, Y., WANG, K., TAN, H.-J. & TIAN, Y. 2025*b* Design concept of compression wave and opposite cowl shock configuration for hypersonic inlet with inward deflecting cowl. *Phys. Fluids* **37** (12), 126116.

TAO, Y., LIU, W., FAN, X., XIONG, B., YU, J. & SUN, M. 2017 A study of the asymmetric shock reflection configurations in steady flows. *J. Fluid Mech.* **825**, 1–15.

TIAN, Z.W. 2024 A study of conical and curved shock waves via the streamline transformation method. *Phys. Fluids* **36** (9), 096117.

VON NEUMANN, J. 1943 Oblique reflection of shock waves. *Explos. Res. Rep.* 12. Navy Department, Bureau of Ordnance.

https://doi.org/10.1017/jfm.2026.11449 Published online by Cambridge University Press

VON NEUMANN, J. 1945 Refraction, intersection and reflection of shock waves. *NAVORD Rep.* 203–45. Navy Department, Bureau of Ordnance.

VUILLON, J., ZEITOUN, D. & BEN-DOR, G. 1995 Reconsideration of oblique shock wave reflections in steady flows. Part 2. Numerical investigation. *J. Fluid Mech.* **301**, 37–50.

WANG, H., ZHAI, Z. & LUO, X. 2021 Reflection of a converging shock over a double curved wedge. *Shock Waves* **31** (5), 439–455.

WANG, H., ZHAI, Z. & LUO, X. 2022 Prediction of triple point trajectory on two-dimensional unsteady shock reflection over single surfaces. *J. Fluid Mech.* **947**, A42.

WANG, H., ZHAI, Z., LUO, X., YANG, J. & LU, X. 2017 A specially curved wedge for eliminating wedge angle effect in unsteady shock reflection. *Phys. Fluids* **29** (8), 086103.

WU, S., XUE, L., MA, Z., LI, W., HOU, P., JIAO, Y., CHENG, K. & WANG, C. 2025 On the asymmetry of over-expansion flows in planar nozzles. *J. Fluid Mech.* **1016**, A42.

XIE, W.-Z., WU, Z.-M., YU, A.-Y. & GUO, S. 2018 Control of severe shock-wave/boundary-layer interactions in hypersonic inlets. *J. Propul. Power* **34** (3), 614–623.

YAN, H., HAN, X., XIONG, H., SHI, C. & YOU, Y. 2024 Curved detonation and its reflections. *J. Fluid Mech.* **984**, A11.

YASUNOBU, T., MATSUOKA, K., KASHIMURA, H., MATSUO, S. & SETOGUCHI, T. 2006 Numerical study for hysteresis phenomena of shock wave reflection in overexpanded axisymmetric supersonic jet. *J. Therm. Sci.* **15** (3), 220–225.

ZHANG, T., HU, W., DA, X., SHI, C., ZHU, C. & YOU, Y. 2024 Fully appreciating the impossibility of shock wave regular reflection from the axis of symmetry in axisymmetric internal flows. *Phys. Fluids* **36** (7), 076110.

ZHANG, T., XU, K., SHI, C., ZHU, C. & YOU, Y. 2023 Reflection and transition of planar curved shock waves. *J. Fluid Mech.* **959**, A11.

https://doi.org/10.1017/jfm.2026.11449 Published online by Cambridge University Press